Thesis for The Degree of Doctor of Philosophy
in Thermo and Fluid Dynamics

Flow in contra-rotating pump-turbines at stationary, transient, and cavitating conditions

Jonathan Fahlbeck

Department of Mechanics and Maritime Sciences
CHALMERS UNIVERSITY OF TECHNOLOGY
Göteborg, Sweden 2024

Flow in contra-rotating pump-turbines at stationary, transient, and cavitating conditions
Jonathan Fahlbeck
ISBN 978-91-8103-077-8

Doktorsavhandlingar vid Chalmers tekniska högskola
Ny serie nr. 5535
ISSN 0346-718X

Department of Mechanics and Maritime Sciences
Division of Fluid Dynamics
Chalmers University of Technology
SE-412 96 Göteborg
Sweden
Phone: +46 (0)31-772 1000

Cover:
Render of contra-rotating pump-turbine in pump mode, with streamlines of relative velocity in red, iso-surface of liquid volume fraction in green-cyan, and iso-surface of Q-criterion in blue.

Printed by Chalmers Digitaltryck
Göteborg, Sweden 2024

Flow in contra-rotating pump-turbines at stationary, transient, and cavitating conditions

Jonathan Fahlbeck

Department of Mechanics and Maritime Sciences
Division of Fluid Dynamics
Chalmers University of Technology

Abstract

This thesis investigates contra-rotating pump-turbines (CRPT) through computational fluid dynamics (CFD) simulations. The research was carried out within the ALPHEUS EU research project, which examined low-head pumped hydro storage using CRPTs. The aim is to analyse and suggest operations for the CRPT at stationary, transient, and cavitating flow conditions. Stationary conditions are analysed using steady-state and unsteady CFD. It is found that the CRPT can produce a hydraulic efficiency of about 90% in both pump and turbine modes for a wide range of operating conditions. Transient startup and shutdown sequences are extensively analysed with the objective of finding load gradient limiting sequences. It is uncovered that the transient sequences in pump mode are more severe than those in turbine mode. This is partly because reversed flow is encountered when the CRPT is not able to overcome the elevation difference between the reservoirs. Therefore, it is suggested that a valve needs to be part of the sequences to avoid reversed flow and control the change in flow rate. For an optimal pump mode startup, the runners need to initially speed up so that the CRPT precisely balance the reservoirs' elevation difference. In the remaining part of the sequence, the valve should open during about three-quarters of the sequence. The runner facing the lower reservoir should use most of the sequence to speed up, while the runner facing the upper reservoir should speed up in the final third of the sequence. For the pump mode shutdown, the valve should close before speeding down the runners, or the runners can speed down as the valve is almost closed. Corresponding sequences in turbine mode are also examined. The suggested startup sequence in turbine mode consists of an initial valve opening, shortly followed by the simultaneous speedup of the runners. The turbine mode shutdown, on the other hand, utilises a multi-stage valve closure as the runners are brought to a standstill. Cavitating flow simulations are carried out at stationary operating conditions in both pump and turbine modes to determine how cavitation impacts the performance of the CRPT. It is found that the pump mode is more sensitive to cavitation than the turbine mode. Nonetheless, irrespective of the mode, the presence of cavitation invariably leads to a degradation in the CRPT performance. This is because the cavitating region causes flow separation on the runner blades, which disturbs the efficient flow guidance in the blade passages.

Keywords: Pumped hydro storage; Low-head; Contra-rotating; Pump-turbine; Startup; Shutdown; Mode-switching; Cavitation; CFD; OpenFOAM

To my family

Acknowledgements

First and foremost, I would like to express my gratitude to my examiner and main supervisor, Håkan Nilsson, for providing me with the opportunity to pursue a PhD. I would also like to thank my co-supervisor, Saeed Salehi. Håkan and Saeed, our countless discussions and the wealth of constructive feedback you provided have been instrumental in my progression and development as a researcher. Furthermore, I extend my thanks to all colleagues and staff at the Department of Mechanics and Maritime Sciences, Division of Fluid Dynamics, at Chalmers University of Technology.

I would also like to acknowledge the ALPHEUS, EU Horizon 2020, project (grant agreement No. 883553) for financing my research. From the ALPHEUS project, I would especially like to express my gratitude to Ruben Ansorena-Ruiz, Justus Hoffstädt, Daan Truijen, Melvin Joseph, and Mehrdad Zangeneh. I am delighted with our constructive meetings and seamless collaboration, which undoubtedly enabled the stable progress of the ALPHEUS project.

I extend my thanks to the National Academic Infrastructure for Supercomputing in Sweden (NAISS), formerly known as the Swedish National Infrastructure for Computing (SNIC), at NSC and C3SE. This infrastructure organisation for high-performance computing, partially funded by the Swedish Research Council through grant agreement No. 2022-06725, has provided the computational resources necessary for my research. Without your computer clusters, the numerical simulations conducted in my research would not have been possible.

Last but certainly not least, I am deeply grateful to my wonderful wife, Gudrun Fahlbeck. Thank you for showing such a keen interest in my work and for the insightful questions you pose when we discuss my research. Your support has been invaluable. You and our, at the time of my defence, 38-day-old daughter Ruth are my life.

Jonathan Fahlbeck
Göteborg, September 2024

Nomenclature

Acronyms

ALPHEUS	Augmenting grid stability through low head pumped hydro energy utilization and storage
BEP	Best efficiency point
CD	Central difference
CFD	Computational fluid dynamics
CRPT	Contra-rotating pump-turbine
IEA	International energy agency
IRENA	International renewable energy agency
LU	Linear-upwind
LUST	Linear-upwind stabilised transport
MOC	Method of characteristics
MOI	Method of implicit
MRF	Multiple reference frame
NPSE	Net positive suction energy
NZE	Net zero emissions by 2050
PHS	Pumped hydro storage
RANS	Reynolds-averaged Navier-Stokes
SAS	Scale adaptive simulation
SST	Shear stress transport

Greek symbols

α_V	Valve opening	$^\circ$
η	Efficiency	%
ν	Fluid kinematic viscosity	m^2/s
Ω	Angular velocity	rad/s
ω	Specific rate of dissipation	$1/s$
ϕ	Arbitrary quantity	–
ρ	Fluid density	kg/m^3
σ	Thoma number	–

Roman symbols

$\boldsymbol{n}$	Normal vector	–
$\boldsymbol{S}_f$	Face area vector	m^2
A	Area	m^2
D	Diameter	m
e	Energy	$kg \cdot m^2/s^2$
F	Force	N
g	Gravitational acceleration	m/s^2
H	Head	m
h	Elevation difference	m
k	Turbulent kinetic energy, Local loss coefficient	m^2/s^2, –
L	Length scale	m
n	Rotational speed	rpm
n_{11}	Speed factor	rpm
P	Power	W

p	Pressure	$\mathrm{kg}/(\mathrm{m}\cdot\mathrm{s}^2)$
Q	Volumetric flow rate	m^3/s
Q_{11}	Flow rate factor	m^3/s
T	Torque	$\mathrm{N}\cdot\mathrm{m}$
t	Time	s
u	Velocity	m/s
V	Volume	m^3
w	Relative velocity	m/s
x	Spatial direction	m
r	Runner speed ratio	–

Subscripts

θ	Tangential direction
z	Axial direction, Location in vertical direction
abs	Absolute
d	Downstream
f	Face, Friction loss
Far	Location far from boundary
g	Gross
l	Local loss
LP	Low-pressure boundary
P	Pump, Patch
R1	Runner 1
R2	Runner 2
rel	Relative
T	Turbine
t	Turbulent
th	Theoretical
u	Upstream
V	Valve
v	Vapour

List of publications

This thesis is based on the following publications:

Paper A J. Fahlbeck, H. Nilsson, S. Salehi, M. Zangeneh, M. Joseph, Numerical analysis of an initial design of a counter-rotating pump-turbine, *IOP Conference Series: Earth and Environmental Science* **774** (1) (2021) p. 012066. DOI: 10.1088/1755-1315/774/1/012066. Conference: *30th IAHR Symposium on Hydraulic Machinery and Systems*, (Online) Lausanne, Switzerland (2021, March 21–26)

Paper B J. Fahlbeck, H. Nilsson, S. Salehi, Flow Characteristics of Preliminary Shutdown and Startup Sequences for a Model Counter-Rotating Pump-Turbine, *Energies* **14** (12) (2021) p. 3593. DOI: 10.3390/en14123593

Paper C J. Fahlbeck, H. Nilsson, S. Salehi, A Head Loss Pressure Boundary Condition for Hydraulic Systems, *OpenFOAM Journal* **2** (2022) pp. 1–12. DOI: 10.51560/ofj.v2.69

Paper D J. Fahlbeck, H. Nilsson, S. Salehi, Evaluation of startup time for a model contra-rotating pump-turbine in pump-mode, *IOP Conference Series: Earth and Environmental Science* **1079** (1) (2022) p. 012034. DOI: 10.1088/1755-1315/1079/1/012034. Conference: *31st IAHR Symposium on Hydraulic Machinery and Systems*, Trondheim, Norway (2022, June 26–July 1)

Paper E J. Fahlbeck, H. Nilsson, S. Salehi, Surrogate based optimisation of a pump mode startup sequence for a contra-rotating pump-turbine using a genetic algorithm and computational fluid dynamics, *Journal of Energy Storage* **62** (2023) p. 106902. DOI: 10.1016/j.est.2023.106902

Paper F J. Fahlbeck, H. Nilsson, S. Salehi, On the pump mode shutdown sequence for a model contra-rotating pump-turbine, *IOP Conference Series: Earth and Environmental Science*, under review. Conference: *9th IAHR Meeting of the WorkGroup on Cavitation and Dynamic Problems in Hydraulic Machinery and Systems*, Timişoara, Romania (2023, October 10–12)

Paper G J. Fahlbeck, H. Nilsson, S. Salehi, Analysis of mode-switching of a contra-rotating pump-turbine based on load gradient limiting shutdown and startup sequences, *IOP Conference Series: Earth and Environmental Science*, accepted. Conference: *32nd IAHR Symposium on Hydraulic Machinery and Systems*, Roorkee, India (2024, September 11–14)

Paper H J. Fahlbeck, H. Nilsson, S. Salehi, M. H. Arabnejad, Performance characteristics of a contra-rotating pump-turbine in turbine and pump modes under cavitating flow conditions, *Submitted for journal publication*, under review.

Additional relevant publications

The following relevant publications are co-authored by Jonathan Fahlbeck. However, they are not appended to, nor part of, this thesis.

Paper I M. Qudaih, B. Engel, D. P. K. Truijen, J. D. M. De Kooning, K. Stockman, J. P. Hoffstaedt, A. J. Laguna, R. Ansorena-Ruiz, N. Goseberg, J. D. Bricker, J. Fahlbeck, H. Nilsson, L. Bossi, M. Joseph, and M. Zangeneh, The Contribution of Low-Head Pumped Hydro Storage to a Successful Energy Transition, *Proceedings of the Virtual 19th Wind Integration Workshop* (2020).

Paper II J. P. Hoffstaedt, D. P. K. Truijen, J. Fahlbeck, L. H. A. Gans, M. Qudaih, A. J. Laguna, J. D. M. De Kooning, K. Stockman, H. Nilsson, P.T. Storli, B. Engel, M. Marence, J. D. Bricker, Low-head pumped hydro storage: A review of applicable technologies for design, grid integration, control and modelling, *Renewable and Sustainable Energy Reviews* **158** (2022) p. 112119. DOI: 10.1016/j.rser.2022.112119

Paper III H. Adebi, C. I. Uribe, J. Fahlbeck, H. Nilsson, Development of Blade Element Momentum (BEM) Method for Hydropower, *IOP Conference Series: Earth and Environmental Science* **1079** (1) (2022) p. 012014. DOI: 10.1088/1755-1315/1079/1/012014

Paper IV J. P. Hoffstaedt, A. J. Laguna, J. Fahlbeck, H. Nilsson, System model development and numerical simulation of low-head pumped hydro storage, *Trends in Renewable Energies Offshore* (2022) pp. 757-763. DOI: 10.1201/9781003360773-85

Paper V D. P. K. Truijen, J. P. Hoffstaedt, J. Fahlbeck, A. J. Laguna, H. Nilsson, K. Stockman, J. D. M. De Kooning, Hardware-in-the-Loop Emulator Test-Setup for a Dual-Rotor Contra-Rotating Pump-Turbine, *IET Conference Proceedings* (2024) pp. 81-88. DOI: 10.1049/icp.2024.2140

Paper VI D. P. K. Truijen, J. P. Hoffstaedt, J. Fahlbeck, A. J. Laguna, H. Nilsson, K. Stockman, J. D. M. De Kooning, Impact of Dual Variable Speed and Inlet Valve Control on the Efficiency and Operating Range of Low-Head Contra-Rotating Pump-Turbines, *IEEE Access* **12** (2024) pp. 86854-86868. DOI: 10.1109/ACCESS.2024.3416679

Paper VII J. P. Hoffstaedt, D. P. K. Truijen, A. J. Laguna, J. D. M. De Kooning, K. Stockman, J. Fahlbeck, H. Nilsson, Low-Head Pumped Hydro Storage: An Evaluation of Energy Balancing and Frequency Support, *Submitted for journal publication*, under review.

Paper VIII J. P. Hoffstaedt, A. J. Laguna, R. Ansorena-Ruiz, D. Schürenkamp, N. Goseberg, D. P. K. Truijen, J. D. M. De Kooning, K. Stockman, J. Fahlbeck, H. Nilsson, Low-head Pumped Hydro Storage using a Contra-Rotating Pump-Turbine: Experimental Investigation and Numerical Model Validation, *Submitted for journal publication*, under review.

Conference presentations without publication

The following works have been presented at international conferences by Jonathan Fahlbeck. However, these presentations did not include a conference paper and are not appended to, nor part of, this thesis.

Conference I J. Fahlbeck, H. Nilsson, S. Salehi, Numerical simulations of counter-rotating pump-turbine with a new head-loss pressure boundary condition, *16th OpenFOAM Workshop*, (Online) Dublin, Ireland (2021, June 8–11).

Conference II J. Fahlbeck, H. Nilsson, S. Salehi, A low-head counter-rotating pump-turbine at unsteady conditions, *17th OpenFOAM Workshop*, Cambridge, United Kingdom (2022, July 10–14).

Conference III J. Fahlbeck, H. Nilsson, S. Salehi, M. H. Arabnejad, Cavitation simulations of a low head contra-rotating pump-turbine, *18th OpenFOAM Workshop*, Genoa, Italy (2023, July 11–14).

Contents

Extended summary

Chapter 1

Introduction

Our current lifestyle results in global warming caused by greenhouse gas emissions [1]. One of the solutions to reduce those emissions and keep global warming within 1.5°C is to increase the usage of renewable sources of energy for the production of electrical energy [2]. An outcome of the COP28 meeting in 2023 is that the globally installed capacity of renewable sources of energy must triple from today's 3870 GW to 11 174 GW by 2030 to keep within the net zero emissions by 2050 (NZE) scenario [3]. The vast majority of this increase is estimated to come from solar and wind power. Fig. 1.1 shows the International Energy Agency (IEA) roadmap for the production of electrical energy required to meet the NZE scenario. By the year 2050, the total installed capacity for the production of electrical energy needs to be increased by more than two-and-a-half times today's levels [4]. Furthermore, it is estimated that solar and wind power alone will contribute to about 70% of the entire production of electrical energy by 2050. However, the electrical energy generated by these types of renewable sources varies over time due to changes in weather conditions and sunlight. An alternative to compensate for the inherent intermittency in the production of electrical energy from these intermittent energy sources is the usage of energy storage [3, 4].

The concept of energy storage is that at times of low demand and high production levels of electrical energy, the excess energy can be put into storage. When the requirements from the electrical grid change and instead there is a high demand in relation to the production capabilities, the stored energy can be utilised and fed back into the grid [6, 7]. This means that an energy storage facility can never by itself act as a net producer of electrical energy to the electrical grid. Instead, energy storage is used to compensate for demand and production capabilities from the electrical grid. Therefore, the key with energy storage is to achieve a large storage capacity and a high conversion efficiency when storing and utilising energy.

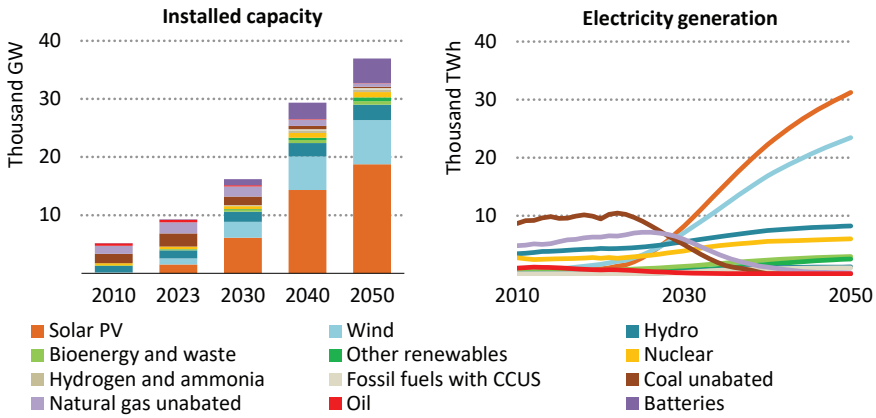

Figure 1.1: Required installed capacity (left) and electricity generation by source (right) to meet the NZE scenario according to IEA. Figure from [4], licensed under CC BY 4.0 [5].

1.1 Energy storage technologies

There are several energy storage technologies, and a few researchers have categorised four different types of systems based on thermal, chemical/electrochemical, mechanical, and electrical processes [6–10]. Thermal energy storage is based on storing the heat, or thermal potential, typically through high-temperature heat accumulators or liquid-air systems. In the chemical or electrochemical category, the storage is made through chemical processes. This category includes for instance hydrogen and battery energy storage. The mechanical solutions store through potential or kinetic energy. Among the potential energy storage, pumped hydro storage (PHS), compressed air systems, and gravity storage are a few alternatives. The kinetic energy storage typically consists of a flywheel. In the final category, electrical processes, the electrical potential is stored through supercapacitors.

PHS from the mechanical – potential energy category is the most common form of energy storage today. PHS was in the year 2020 responsible for 90.3% of the world's energy storage capacity [11]. This was equivalent to a total power of 160 GW [12]. The International Renewable Energy Agency (IRENA) stated in 2020 that to achieve the NZE scenario, the installed power capacity of PHS needs to double by 2050, reaching 325 GW [2]. This is to cope with the rising intermittent energy sources. By the year 2023, the installed power capacity reached 179 GW [13], showing an increase of the globally installed PHS capacity by 11.9% since 2020.

A PHS power plant consists of at least two large water reservoirs at different height elevations, as illustrated in Fig. 1.2. The reservoirs are connected via pipelines to move water between them. Potential energy is stored by pumping water from the lower to the upper reservoir [14]. The energy is utilised by releasing water from the upper to the lower reservoir through a

turbine connected to a generator. The theoretical power for PHS depends on the difference in height elevations and the volumetric flow rate [15] as

$$P_{\text{th}} = \rho g h Q. \tag{1.1}$$

Here ρ is the fluid density, g is the gravitational acceleration, h represents the elevation difference between the reservoirs, usually referred to as the gross head (H_{g}), and Q is the volumetric flow rate. The storage capacity can, in simple terms, be expressed by the difference in height elevations and the volume of water (V) in the upper reservoir as

$$e = \rho g h V. \tag{1.2}$$

Note however that this expression assumes that all of the water is located at h. The cycle efficiency of PHS usually varies around 70–80% for various sites [16], and it has been concluded that PHS is the most effective type of energy storage system [10].

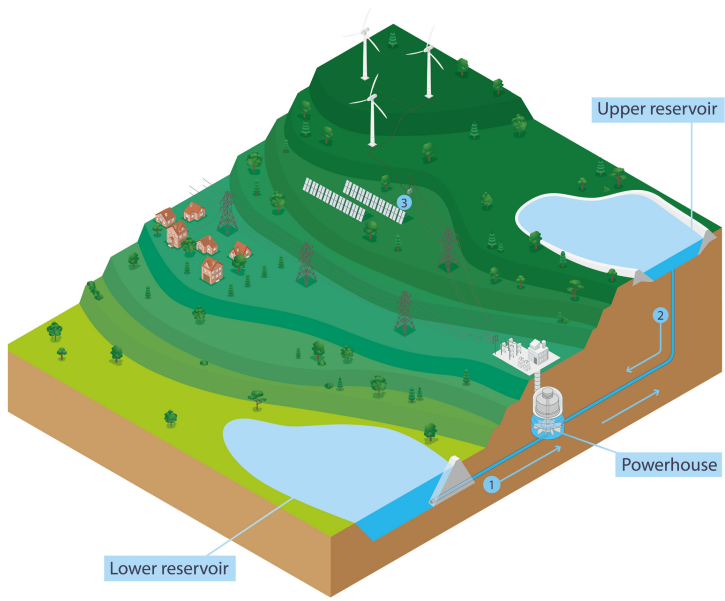

Figure 1.2: Conceptual view of pumped hydro storage. Figure used with permission from the International Hydropower Association [17, 18].

Because the power, Eq. (1.1), and storage capacity, Eq. (1.2), for PHS depends on the elevation difference, PHS has conventionally been restricted to high mountain areas, where large elevation differences are available [19]. However, due to limited power distribution capacity, energy storage is also needed in regions lacking appropriate topographical conditions. This brings a need for complementary storage technologies.

Several researchers highlight that batteries, lithium-ion in particular, are one of the most promising emerging energy storage technologies because of

recent technological advancements and expected price reductions [7, 9, 10, 16]. Battery energy storage systems have comparably high cycle efficiency, around 78–88% for lithium-ion batteries [20]. However, battery energy storage has a limited lifetime, and its capacity deteriorates with the number of cycles. Another disadvantage with batteries is the large emissions connected to mining materials and/or manufacturing processes [9].

Compressed air and hydrogen energy storage are additional alternatives highlighted as potential solutions for bulk energy storage [7, 9, 16]. Compressed air energy storage is a mature technology that presents a cycle efficiency of 42–73% as well as a long lifetime [16, 20]. The main drawbacks of compressed air energy storage are the large variation in cycle efficiency and geographical constraints [16]. For hydrogen energy storage, a cycle efficiency of around 35–42% is anticipated while having a shorter expected lifetime than compressed air energy storage [20]. Hydrogen energy storage is deemed to have the potential to revolutionise energy storage in the future. On the other hand, substantial economic and technological challenges remain before hydrogen energy storage can be realised on a feasible scale [7, 9, 16, 20].

Another alternative for energy storage is to design PHS that is not constrained by the need for a specific topography with high mountain areas. This involves reducing the required elevation difference between the reservoirs. Consequently, to achieve a power similar to that of conventional PHS, the flow rate must be increased as shown by Eq. (1.1). In addition, to store a comparable amount of energy, the size of the reservoirs must also increase as demonstrated by Eq. (1.2). Therefore, to achieve energy storage comparable to traditional PHS in regions with flat topography, innovative PHS designs are required. These PHS designs would accommodate higher flow rates, smaller elevation differences, and larger reservoirs [21]. This variant of PHS is referred to as 'low-head' PHS, indicating a minimal elevation difference between the reservoirs.

1.2 Low-head pumped hydro storage

The present work is concerned with low-head pumped hydro storage. The term low-head is not unambiguously determined in the research community. In this thesis it is defined according to the constraints of the ALPHEUS (Augmenting Grid Stability Through Low Head Pumped Hydro Energy Utilization and Storage) EU research project [22, 23], which the majority of the present work is conducted within. In the ALPHEUS project, novel reversible pump-turbines (RPT) are explored for elevation differences between 2–20 m. Thus, the definition of low-head PHS within this thesis is that the difference in height elevations between the reservoirs should be a maximum of 20 m.

The general principles of low-head PHS are the same as those of conventional PHS. This means that energy is stored and utilised by pumping water to an upper reservoir for storage and released from the upper reservoir to extract energy. In the scope of the ALPHEUS project, the RPT unit should have a nominal power of approximately 10 MW. By using Eq. (1.1) and assuming an elevation difference of 9 m, this leads to a nominal flow rate of nearly 115 m^3/s

per RPT unit. The comparably large flow rate of low-head PHS impacts the size of the reservoirs, as the flow rate dictates how fast the reservoirs are emptied and filled. The ALPHEUS project explores the potential of constructing low-head PHS in shallow sea areas. Thereby, the sea is used as the upper reservoir, and the lower reservoir is arranged in a man-made so-called energy island.

To determine an appropriate type of RPT unit for low-head high-flow conditions, the specific speed parameter,

$$\Omega_\mathrm{s} = \frac{\Omega Q^{0.5}}{(gH)^{0.75}},$$

can be used. Here Ω is the angular velocity of the RPT, and H is the RPT net head (see Section 2.3). As indicated in Fig. 1.3, the specific speed influences the runner geometry. The low-head high-flow conditions mean that an axial-flow RPT configuration is the most appropriate [24].

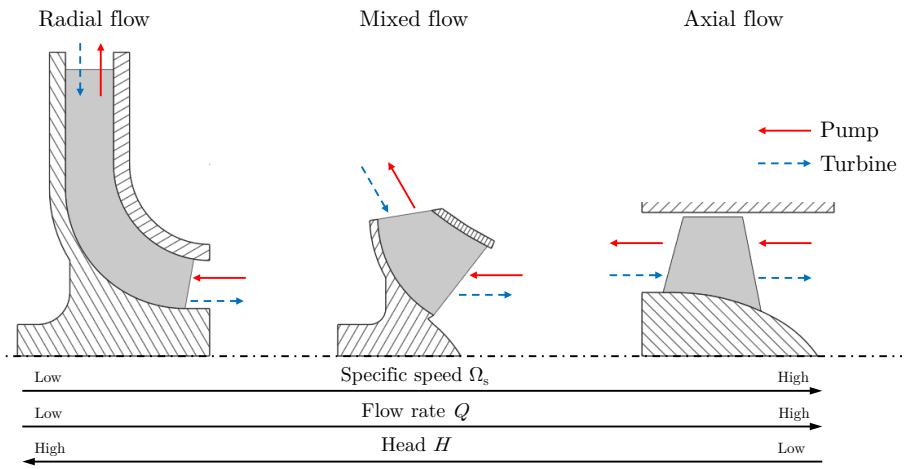

Figure 1.3: Runner geometries as a function of specific speed Ω_s, flow rate Q and net head H. Adapted from [21], licensed under CC BY 4.0 [5].

Given that axial-flow machines are preferable for low-head high-flow conditions, axial-flow RPT units are investigated in the ALPHEUS project. More specifically, axial-flow contra-rotating pump-turbines (CRPT), see Chapter 2 for a description, are one of the examined configurations. A CRPT consists of two runners rotating in opposite directions, hence the name contra-rotating. The main reason for not using a single-runner configuration is that a CRPT presents a wider range of operations at high efficiency and can be of smaller size [25]. Using single-runner configurations through a pump-as-turbine or a turbine-as-pump is also possible. However, the efficiency and operating range of such machines is typically low in the mode (pump or turbine) that it is not designed for [26–29]. An example of this is the La Rance tidal plant, constructed in the 1960s, where axial flow bulb turbines are installed with a rated hydraulic efficiency of 86% in turbine mode whereas only 66% in pump mode [15, 29, 30]. Another example is the Kislaya Guba tidal plant, which

originally also used an axial flow bulb turbine with a maximum turbine mode efficiency of 86%, whereas 67% in pump mode [30].

The CRPT within the context of hydropower is a relatively new concept [31], and it is currently not used as a PHS pump-turbine unit. Various researchers have proposed the CRPT as a viable alternative for low-head PHS [21, 29, 32], or as an energy recovery unit in water supply systems [33]. The primary development of CRPTs has predominantly focused on optimising the blade geometries under stationary and non-cavitating flow conditions. However, due to the rise of intermittent energy sources, transient operations occur more frequently as hydropower and PHS need to balance the production of electrical energy to ensure a stable grid [34, 35]. This makes it relevant to investigate how to perform transient operations that minimise unfavourable transient conditions of the CRPT as this knowledge is presently slim.

Furthermore, investigations of cavitating flow conditions for the CRPT are scarce. It has been suggested that a CRPT should have improved cavitation characteristics compared to a single-runner configuration [25, 36]. In a design optimisation study of a CRPT [37], the researchers reduced the rotational speed to avoid cavitation. When they redesigned their CRPT, only single-phase flows were considered and no analysis was made that could capture cavitation. Thus, the mechanism by which the performance is impacted by cavitation remains limited for the CRPT.

1.3 Objectives and delimitations

The CRPT developed in the ALPHEUS project has to be analysed to understand the working mechanisms and how to maximise usability. Therefore, this thesis focuses on three main objectives connected to the CRPT, which are:

I Understand the flow characteristics and working principles at stationary and transient conditions.

II Identify and propose startup and shutdown sequences that limit load gradients.

III Understand how and why cavitation affects the performance at stationary conditions.

The first objective at stationary conditions is of interest to highlight how and in which conditions the CRPT should operate. The focus is on identifying efficiency, operational span, and flow characteristics. The second objective concerns the flexibility of the CRPT. To have an effective energy storage plant, the pump-turbine must be able to quickly adapt to demand variations from the electrical grid. On the other hand, adverse transient operations account for the majority of harmful conditions and can have a direct negative impact on the lifespan of the pump-turbine [34, 35, 38]. Given that a PHS station may change its operational mode multiple times within a day, it becomes crucial to understand how to execute transient operations of the pump-turbine unit. This knowledge is key to limiting adverse load conditions during the

transient operations, thereby improving flexibility and minimising premature deterioration [39]. The third objective is connected to the first objective since both concern the continuous operation of the CRPT. It is well known that cavitation can reduce the lifetime and degrade the operating performance of conventional pump-turbines [40, 41]. It is for that reason of importance to investigate how cavitation impacts the performance of the CRPT and which operating conditions to avoid.

Computational fluid dynamics (CFD) is the primary tool used to analyse the flow field of the CRPT. The simulations in the present work are performed using the unsteady Reynolds-averaged Navier-Stokes (RANS) equations. To answer the proposed objectives, Paper A, and Sections 2.1 and 2.3, concern the stationary operation of the CRPT. Transient operations are analysed in Papers B, D–G, as well as in Sections 4.2 and 4.3. The developments presented in Paper C are used in Papers D–G to achieve more realistic flow conditions compared to Paper B. Finally, how cavitation affects the CRPT's operating capabilities is investigated in Paper H and Section 4.4.

This thesis does not cover the design and optimisation work carried out to derive blade geometries, as partners of the ALPHEUS project have done that work. Furthermore, the experimental measurement work carried out in the ALPHEUS project has not been made as a part of this thesis. Because the experimental tests were severely delayed, no extensive validation campaign could be carried out as described in Section 3.2.1. Further, this thesis does not cover the socioeconomic and environmental aspects of low-head PHS.

Chapter 2

Contra-rotating pump-turbine

This chapter encompasses the design and working principles of the evaluated CRPT from the ALPHEUS project. It should be noted that this thesis does not include designing the blade geometries or the mechanical components, as partners in the ALPHEUS project focused on that.

Figure 2.1 shows the model scale CRPT geometry, including the mounting arrangement and conceptual mechanical components, assumed for Papers F–H. The layout is according to the experimental test facility at TU Braunschweig, where partners experimentally tested the machine as part of the ALPHEUS project. In Papers D and E, the blade geometries are identical to those shown in Fig. 2.1, however a preliminary mounting arrangement was assumed. More details about the mounting arrangements are given in Section 2.2. In Papers A and B, slightly different blade geometries were used based on a preliminary design.

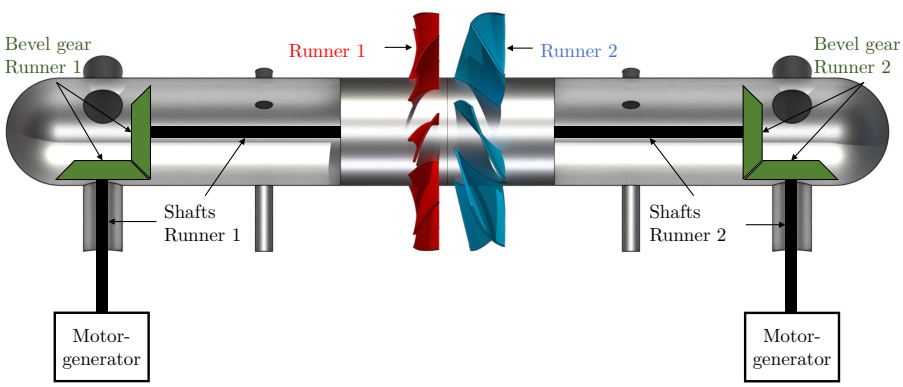

Figure 2.1: Main components of the studied CRPT. The flow is from right to left in turbine mode and left to right in pump mode.

In common for all studies, except parts of Papers A and C, is that a model scale CRPT geometry is evaluated. The shroud diameter is around 270 mm in all studies, and the runners' nominal rotational speed is in the order of 500–1500 revolutions per minute (rpm). Additionally, Runner 1 (red) is the low-pressure runner, has eight blades and is located upstream in pump mode and downstream in turbine mode. Runner 2 (blue) is the high-pressure runner, has seven blades and is placed downstream in pump mode and upstream in turbine mode. Furthermore, each runner is connected to an individual shaft to transfer torque, through the bevel gear, between a variable-speed motor-generator unit and the runner. Note that the depicted shaft alignment in Fig. 2.1 is for the model scale geometry only. At the prototype scale, the recommendation from the ALPHEUS project is to use bulbs to house the motor-generator units.

As a side note, the terms 'contra-rotating' and 'counter-rotating' are frequently used interchangeably within the hydropower research community when referring to the same configuration. This is also true for the author of this thesis. In the earlier publications (Papers A and B), the term 'counter-rotating' is used, while in the later works (Papers D to H), the term 'contra-rotating' is employed. The reason for this is that, within aeronautical propulsion systems, 'contra-rotating' refers to two propellers fitted on a coaxial shaft rotating in opposite directions. However, 'counter-rotating' is used for a twin- or multi-engine aircraft, where the propellers on each side of the aircraft rotate in opposite directions. Therefore, the term 'contra-rotating' aligns more closely with the terminology used in other industries for the type of pump-turbine configuration investigated in this thesis.

2.1 Working principles

The general mechanism of the CRPT is explained by the velocity triangles in Fig. 2.2. The machine is designed for a pure axial inflow in both pump and turbine modes. Thereby avoiding the usage of guide vanes for the CRPT. The upstream runner swirls the flow, while the downstream runner de-swirls the flow, making the flow axial downstream of the machine at the best efficiency points (BEP). In the description below, the velocity concerns the tangential component as the axial component remains constant. However, this is left out for the brevity of the text.

In pump mode, indicated as solid arrows in Fig. 2.2, the flow is from left to right. A pump needs to create a sufficient pressure increase to drive the flow from a lower to an upper reservoir. This is achieved by converting kinetic energy into pressure over the rotating runners. The runners are made to rotate by electric motors, which transfer torque to the runners. The added torque to the flow over Runner 1 (upstream in pump mode) results in a deceleration of the relative velocity over the runner. As a result, a clockwise swirl component is added to the absolute velocity, as shown in Fig. 2.2. The incoming absolute velocity entering Runner 2 is the same as the absolute velocity leaving Runner 1. Runner 2 is thus designed for an absolute velocity with an incoming clockwise swirl in pump mode. To de-swirl the flow, the rotational direction of Runner 2

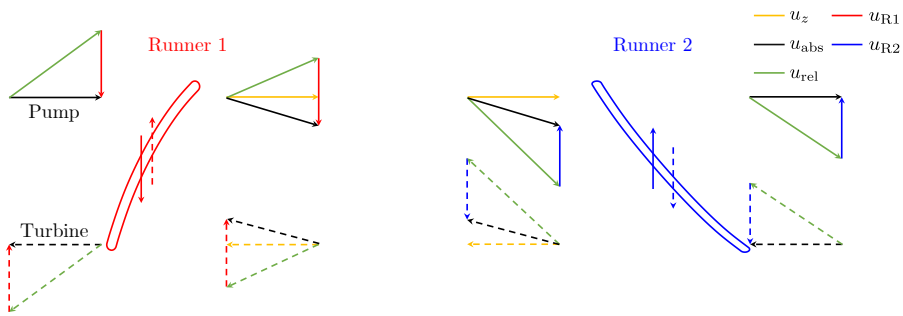

Figure 2.2: Schematic view of velocity triangles of the CRPT in pump mode (solid arrows) and turbine mode (dashed arrows). Subscripts: abs denotes absolute, rel denotes relative, z represents the axial direction (positive in pump mode), R1 refers to Runner 1, and R2 refers to Runner 2.

needs to be in the opposite direction to that of Runner 1. Hence, because of the contra-rotational direction of Runner 2, the flow is de-swirled over Runner 2 by decelerating the relative, and absolute, velocity over the runner. The change in kinetic energy, caused by the deceleration of the relative velocity, over both runners is converted into pressure to drive the flow from the lower to the upper reservoir.

The turbine mode operation is opposite to the pump mode operation, as shown by the dashed arrows in Fig. 2.2. In turbine mode, the flow is from an upper reservoir to a lower reservoir, and energy is extracted from the flow. Thus, the available energy in turbine mode is a function of the difference in height elevations between the reservoirs and the hydraulic losses in the conduit. Energy is extracted in turbine mode by converting pressure to kinetic energy by accelerating the relative velocity over the runners. As the flow goes over the Runner 2 blades (upstream in turbine mode), the flow is deflected in the negative tangential direction because of the blade shape. According to Newton's third law of motion, when the flow is deflected in the negative tangential direction by the runner blade, the runner must experience an equally strong angular momentum in the opposite direction. The angular momentum transferred from the flow to the runner makes the runner rotate, and the generator applies a counteracting torque to produce electrical energy. The deflected flow in the negative tangential direction over Runner 2 is realised as an anti-clockwise swirl component of the absolute velocity between the runners. The downstream Runner 1 is designed to make use of the anti-clockwise swirl component by de-swirling the flow, making it axial downstream of Runner 1. Hence, the rotational direction of Runner 1 is opposite to that of Runner 2.

2.2 Geometries of numerical domains

Several different numerical domains have been utilised for the various unsteady and transient CFD studies, as illustrated in Fig. 2.3. These domains were

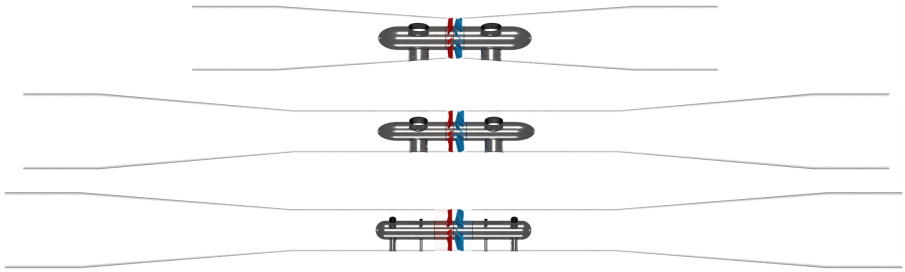

Figure 2.3: Numerical domains used for the unsteady and transient studies. The low-pressure boundary is to the left, and the high-pressure boundary is to the right.

derived and modified based on the planned layout of the experimental test facility where the CRPT was eventually tested. The above geometry is an early draft used in Papers A and B. In that geometry, a runner diameter of 270 mm was assumed. The middle domain, a refined version of the above domain, includes an extended straight section by the runners and uses a runner diameter of 276 mm. This middle domain is used in Papers D and E. The below domain, used in Papers F–H, employs the mounting arrangement according to the experimental test facility at TU Braunschweig. The differences between the below and middle domains include a changed hub shape and the presence of two sets of additional support struts. Additionally, the cone angle of the contraction/expansion parts is slightly reduced.

2.3 Performance parameters

For any pump-turbine, the performance and operating range are important to understand its applicability. The net head, power, and efficiency are three of the most common engineering quantities for pump-turbines.

The net head (H) is a measure of energy extracted (in turbine mode) or added (in pump mode) from/to the system over the pump-turbine unit, expressed in metres. The term gross head (H_g) refers to the hydrostatic pressure difference between two water levels, for example the upper and lower reservoirs. If nothing else is stated in this thesis, the term 'head' refers to the net head. For an axial flow machine placed in the horizontal plane, the net head is defined as

$$H = \frac{\Delta p_0}{\rho g}. \tag{2.1}$$

Here Δp_0 is the total pressure change over the CRPT, ρ is the fluid density, and g is the gravitational acceleration. The total pressure change is calculated based on the average values on planes located just on the low-pressure and high-pressure sides of the CRPT. The exception for this is in Section 4.5, where the pressure change is based on the static pressure from pressure probes/transducers located at the shroud.

Throughout this thesis, the power (P) is always defined by the torque (T) times the runner angular velocity (Ω) as

$$P = \sum_{i=1}^{2} T_{\mathrm{R}i}\Omega_{\mathrm{R}i}. \tag{2.2}$$

Index i is 1 or 2 for the respective runner. The torque is calculated by integrating pressure and viscous forces on the runner blades and the rotating part of the hub.

The efficiency in this work refers to the hydraulic efficiency. This means that losses from the drive-train, motor-generator, or other mechanical components are not considered. The efficiency is calculated as

$$\eta_{\mathrm{T}} = \frac{P}{\rho g H Q}, \quad \eta_{\mathrm{P}} = \frac{\rho g H Q}{P}, \tag{2.3}$$

where subscript T and P are for turbine and pump modes, respectively. The term $\rho g H Q$ can be referred to as the hydraulic power. The hydraulic power is the maximum power available in turbine mode, whereas it is the smallest power that must be overcome in pump mode.

Figure 2.4 presents the engineering quantities at a constant set of runner speeds as a function of flow rate for the model scale CRPT. The head curve (left) shows a stable decrease in pump mode at flow rates larger than 80% of the BEP. The pump power curve (middle) exhibits a similar pattern to the head curve, albeit with a flatter shape. In turbine mode, the head and power increase monotonically with the flow rate. The efficiency curves (right) demonstrate that the model scale CRPT can achieve hydraulic efficiencies close to 90% across a wide range of operating conditions in both modes. In pump mode, the efficiency exceeds 80% at flow rates around 75–115%. In turbine mode, the efficiency surpasses 80% at 85–125% of the BEP flow rate.

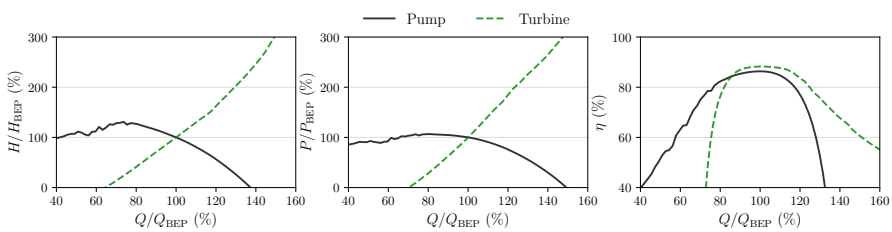

Figure 2.4: Engineering quantities in pump and turbine modes as a function of flow rate at constant runner rotational speeds. The head (left), power (middle), and flow rate are normalised by the BEP. The curves are based on steady-state CFD simulations of the model scale CRPT.

2.4 Operating modes of pump-turbines

The operations of an RPT can be characterised into four quadrants as illustrated in Fig. 2.5. The four-quadrant characterisation provides all possible RPT operating conditions through the flow rate (Q_{11}) and speed (n_{11}) factors [42, 43]. These factors compare the performance of the RPT to a geometrically similar machine with a diameter (D_{11}) and head (H_{11}) equal to 1 m and are defined as

$$Q_{11} = Q\left(\frac{D_{11}}{D}\right)^2 \sqrt{\frac{H_{11}}{H}}, \tag{2.4}$$

$$n_{11} = n\frac{D}{D_{11}}\sqrt{\frac{H_{11}}{H}}. \tag{2.5}$$

Here D is the runner diameter in m, the rotational speed n in rpm, the head H in m, and the flow rate Q in m^3/s.

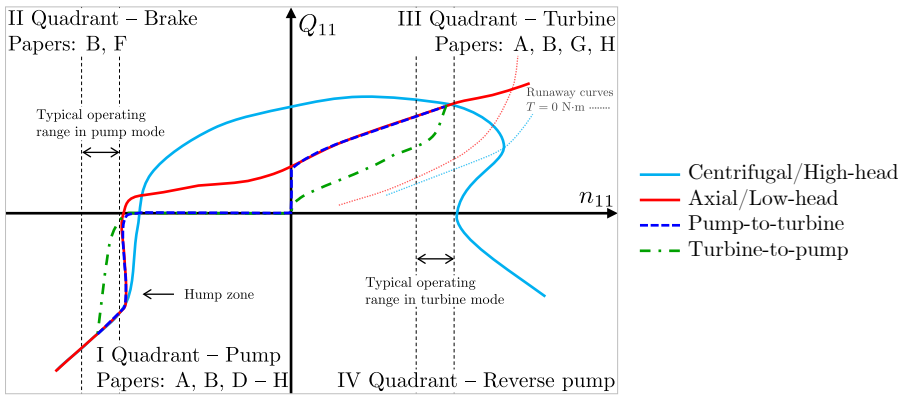

Figure 2.5: Principle illustration of the four-quadrant characterisation of RPT operations. 'Centrifugal/High-head' is a conventional high-head pump-turbine, and 'Axial/Low-head' is based on unsteady simulations of the CRPT. The graph is not to scale for high-head and low-head machines.

The RPT four quadrant operations are characterised by [42–47]:

I Quadrant – Pump:
In this quadrant, continuous and nominal operations occur in pump mode. The flow rate and rotational speed are negative in pump mode since they are defined as positive in turbine mode. The area between the dashed lines represents the typical operating range in pump mode. The right line represents the maximum head of the power plant, or to avoid the unstable hump zone. The left line is the minimum available head and the largest possible flow rate.

II Quadrant – Brake:
In this quadrant, the rotational speed is in the pump mode direction

($n < 0$), whereas the flow rate is in the turbine mode direction ($Q > 0$). This mode is encountered during transient conditions when the pump net head is less than the gross head due to the rotational speed not being sufficiently high. The brake quadrant is typically reached during fast mode-switching of a pump-turbine at constant guide-vane openings. This quadrant can also be reached in the case of power failure in pump mode. The intersection between the I and II quadrants corresponds to the net head – zero-through-flow condition.

III Quadrant – Turbine:
This quadrant is where continuous turbine mode operation occurs. It is characterised by the positive flow rate and rotational speed as the RPT is in generating mode. The turbine mode operation is limited by the maximum (left dashed line) and minimum (right dashed line) available head, as well as the power plant's allowed flow rates.

The transition between the II and III quadrants is denoted as the zero-speed flow rate and break-away torque. In other words, the corresponding flow rate and torque as the runners are at a standstill. To the far right of this quadrant, there is the runaway condition. This is defined as the zero-torque or no-load condition, where the torque is zero. When passing the runaway curve, the RPT experiences a turbine-braking mode as negative torque is delivered to the shaft. For a centrifugal/high-head pump-turbine, the turbine-braking is characterised by $\mathrm{d}Q_{11}/\mathrm{d}n_{11} > 0$. For an axial/low-head pump-turbine, the Q_{11} continues to increase with rising n_{11}.

IV Quadrant – Reverse pump:
In the reverse pump quadrant, the RPT is pumping water in the pump mode direction while the runner rotates in the turbine mode direction. It is characterised by a negative flow rate ($Q < 0$) and positive rotational speed ($n > 0$). This mode is only reached in transient operations for centrifugal/high-head RPTs.

For a centrifugal/high-head RPT, the flow is unstable in the area between the runaway condition in the III quadrant and the IV quadrant. The flow can switch sporadically between generating and pumping modes, which may cause substantial fluctuations in the head, flow rate, and torque.

In Fig. 2.5, the 'Centrifugal/High-head' curve refers to the typical operation of a single unit high-head RPT [45]. The shape of the 'Axial/Low-head' curve is based on unsteady simulations of the CRPT and aligns with the operating cycles of axial flow pumps as outlined by Swanson already in the 1950s [48]. The 'Pump-to-turbine' and 'Turbine-to-pump' curves demonstrate the principal concept of the evaluated mode-switching sequences in Paper G. In this paper, startup and shutdown sequences in each mode are combined to form complete mode-switching sequences. These sequences are derived by combining the outcomes of studies of the pump mode startup in Papers D and E, as well as the pump mode shutdown in Paper F and Section 4.2. The startup and

shutdown sequences in turbine mode are discussed in Section 4.3. The key idea behind the 'Pump-to-turbine' and 'Turbine-to-pump' sequences is to introduce a valve into the sequences, thereby avoiding the II quadrant. This is because Paper B demonstrates that large and rapid load gradients on the runners occur in the transition between the pump and the brake quadrants. Lastly, Papers A and H focus on the stationary operation in pump and turbine modes, and therefore, these studies are in the I and III quadrants.

2.5 Cavitation in pump-turbines

Cavitation is the process in which vapour bubbles form in a liquid when the static pressure falls below the vapour pressure [49]. The formation of cavitation can lead to significant material damage when the vapour bubbles collapse. During the collapse of a bubble, shock waves and microjets may form within the cavity of the collapsing bubble. If a bubble collapses near a solid surface, these phenomena can cause damage or erosion to the material.

In addition to the material damage caused by collapsing bubbles, cavitation can also degrade the operating performance of pump-turbines [40, 41]. In the case of the CRPT, the mechanisms by which cavitation affects its performance are not fully understood. Consequently, the study in Paper H aims to uncover the reasons behind the degradation of the CRPT's operating performance due to cavitating flow.

For pumps and turbines, the Thoma number (σ) can be used to evaluate the cavitation condition. The Thoma number is considered according to IEC 60193 [45] as

$$\sigma = \frac{\mathrm{NPSE}}{\mathrm{E}} = \frac{\frac{p_{\mathrm{LP}} - p_{\mathrm{v}}}{\rho} + \frac{Q^2}{2A_{\mathrm{LP}}^2}}{gH}. \tag{2.6}$$

Here p_{LP} and A_{LP} are the static pressure and the cross-sectional area at the low-pressure side of the machine, respectively, while p_{v} is the vapour pressure. The Thoma number describes the ratio of the net positive suction energy (NPSE) to the specific hydraulic energy of the machine (E). The NPSE is the specific hydraulic energy on the low-pressure side of the machine, subtracted by the hydraulic energy of the vapour pressure (p_{v}/ρ).

Chapter 3

Numerical modelling

This chapter presents the main principles of the 3D CFD simulations used in the different papers and studies presented in this thesis. Note however that some modifications exist in the various studies depending on the objectives.

3.1 Computational fluid dynamics

The CFD simulations conducted in this study utilise the OpenFOAM open-source CFD code [50]. Although various versions of OpenFOAM have been employed across the research, the vast majority is based on the ESI release of OpenFOAM, including versions such as v1912 [51], v2012 [52], etc.

3.1.1 Governing equations

The incompressible unsteady RANS equations are used for the unsteady and transient CFD simulations in this thesis. The unsteady RANS equations read

$$\frac{\partial \bar{u}_i}{\partial x_i} = 0, \tag{3.1}$$

and

$$\underbrace{\frac{\partial \bar{u}_i}{\partial t}}_{\text{temporal}} + \underbrace{\frac{\partial \bar{u}_j \bar{u}_i}{\partial x_j}}_{\text{convection}} = \underbrace{-\frac{1}{\rho}\frac{\partial \bar{p}}{\partial x_i}}_{\text{source}} + \underbrace{\frac{\partial \bar{u}_i}{\partial x_j}\left(\nu \frac{\partial \bar{u}_i}{\partial x_j} - \overline{u_i' u_j'}\right)}_{\text{diffusion}}, \tag{3.2}$$

for continuity and momentum in tensor notation, respectively. In the equations, u is the velocity, x is the spatial direction, p is the pressure, ρ is the fluid density, and ν is the fluid kinematic viscosity. For the cavitating flow simulations presented in Paper H and Section 4.4, the fluid properties ρ and ν are for the fluid mixture. The overline symbol '$\bar{}$' denotes that the quantity is time-average. The unknown Reynolds stress tensor (divided by the density) $\overline{u_i' u_j'}$ is modelled through Boussinesq's assumption, which states

$$\overline{u_i' u_j'} = -\nu_\mathrm{t}\left(\frac{\partial \bar{u}_i}{\partial x_j} + \frac{\partial \bar{u}_j}{\partial x_i}\right) + \frac{2}{3}\delta_{ij}k. \tag{3.3}$$

Here ν_t is the turbulent kinematic viscosity, k is the turbulent kinetic energy and δ_{ij} is the Kronecker delta.

For closure of the RANS equations, Eqs. (3.1) and (3.2), the k-ω SST-SAS (shear stress transport – scale adaptive simulation) turbulence model is used for the unsteady and transient simulations [53, 54]. The turbulent kinetic energy is defined as $k = 0.5\overline{u_i' u_i'}$, and the turbulent kinematic viscosity as

$$\nu_\mathrm{t} = \frac{a_1 k}{\max(a_1\omega, SF_2)} \tag{3.4}$$

in the turbulence model. The OpenFOAM v2112 implementation of the k-ω SST k-equation reads [55]

$$\frac{\partial k}{\partial t} + \frac{\partial \bar{u}_j k}{\partial x_j} = \tilde{P}_k - \beta^* k\omega + \frac{\partial}{\partial x_j}\left[(\nu + \sigma_k \nu_\mathrm{t})\frac{\partial k}{\partial x_j}\right], \tag{3.5}$$

and the specific rate of dissipation ω-equation is

$$\frac{\partial \omega}{\partial t} + \frac{\partial \bar{u}_j \omega}{\partial x_j} = \alpha S^2 - \beta\omega^2 + \frac{\partial}{\partial x_j}\left[(\nu + \sigma_\omega \nu_\mathrm{t})\frac{\partial \omega}{\partial x_j}\right] + 2(1-F_1)\frac{\sigma_{\omega 2}}{\omega}\frac{\partial k}{\partial x_j}\frac{\partial \omega}{\partial x_j}. \tag{3.6}$$

The model coefficients and functions are according to Menter et al. [55].

The SAS modifications to the SST model are made by introducing an additional source term, Q_SAS, into the ω-equation [53, 54, 56]. In OpenFOAM v2112, the Q_SAS term reads [53, 56]

$$Q_\mathrm{SAS} = \max\left[\zeta_2 \kappa S^2 \left(\frac{L}{L_\mathrm{vK}}\right)^2 - C\frac{2k}{\sigma_\Phi}\max\left(\frac{1}{\omega^2}\frac{\partial \omega}{\partial x_j}\frac{\partial \omega}{\partial x_j}, \frac{1}{k^2}\frac{\partial k}{\partial x_j}\frac{\partial k}{\partial x_j}\right), 0\right]. \tag{3.7}$$

Here L is the length scale of the modelled turbulence

$$L = \frac{k^{0.5}}{c_\mu^{0.25}\omega},$$

and L_vK is the von Kármán length scale which is defined as $\kappa|\boldsymbol{u}'/\boldsymbol{u}''|$. The first velocity derivative ($\boldsymbol{u}'$) is expressed as [54]

$$S = \sqrt{2\bar{s}_{ij}\bar{s}_{ij}},$$

where

$$\bar{s}_{ij} = 0.5\left(\frac{\partial \bar{u}_i}{\partial x_j} + \frac{\partial \bar{u}_j}{\partial x_i}\right).$$

The second velocity derivative ($\boldsymbol{u}''$) is described as [54]

$$\boldsymbol{u}'' = \sqrt{\frac{\partial^2 \bar{u}_i}{\partial x_k^2}\frac{\partial^2 \bar{u}_i}{\partial x_j^2}}.$$

The OpenFOAM v2112 implementation of the von Kármán length scale includes dampening of the smallest resolved turbulent fluctuations and reads [56]

$$L_{\mathrm{vK}} = \max\left(\kappa \left|\frac{\boldsymbol{u}'}{\boldsymbol{u}''}\right|, C_{\mathrm{s}}\sqrt{\frac{\kappa\zeta_2}{\beta/\beta^* - \alpha}}\Delta\right). \tag{3.8}$$

Here Δ is the filter width (cubic root of the cell volume). All model coefficients and functions are found in the works by Menter and Egorov [53, 56].

In the cavitating flow simulations presented in Section 4.4 and in Paper H, the Schnerr-Sauer cavitation model [57–59] is employed. In the Schnerr-Sauer model, the fluid is considered a mixture of two fluids and an additional transport equation for the liquid volume fraction is introduced. The liquid volume fraction transport equation includes a mass transfer term accounting for vaporisation and condensation processes. For a mathematical description of the cavitation model, the reader is referred to Section 3.2 of Paper H.

3.1.2 Discretisation schemes

The RANS equations and turbulent quantities are discretised and resolved on a computational mesh. The selection of numerical discretisation schemes frequently represents a balance between the stability and accuracy of the simulation. In this work, no formal studies have been conducted to identify the most suitable sets of schemes. Instead, the selection is based on the experience of the author and the research group.

For a control volume, the general transport equation of an arbitrary scalar, denoted as ϕ, is defined by applying Gauss's divergence theorem ($\int_V \nabla\phi \,\mathrm{d}V = \int_A \phi \cdot \boldsymbol{n} \,\mathrm{d}A$) as [60]

$$\underbrace{\frac{\partial}{\partial t}\int_{\mathrm{V}} \phi \,\mathrm{d}V}_{\text{temporal}} + \underbrace{\int_A (\phi\boldsymbol{u}) \cdot \boldsymbol{n} \,\mathrm{d}A}_{\text{convection}} = \underbrace{\int_A (\Gamma\nabla\phi) \cdot \boldsymbol{n} \,\mathrm{d}A}_{\text{diffusion}} + \underbrace{\int_{\mathrm{V}} S_\phi \,\mathrm{d}V}_{\text{source}}. \tag{3.9}$$

In the equation, V is the volume of the control volume, A is the area/surface of the control volume, $\boldsymbol{n}$ is the area/surface normal, Γ is the diffusion coefficient, and S_ϕ represent source term(s).

The discretisation in time is in the unsteady simulations handled with the backward scheme [61]. The backward scheme is second-order accurate, and the temporal derivative is approximated as

$$\frac{\partial\phi}{\partial t} = \frac{\frac{3}{2}\phi^n - 2\phi^o + \frac{1}{2}\phi^{oo}}{\Delta t}. \tag{3.10}$$

The scheme uses three time instances, which are $\phi(t + \Delta t) = \phi^n$, $\phi(t) = \phi^o$, and $\phi(t - \Delta t) = \phi^{oo}$. A number of publications have been made where the backward scheme is used for Francis and Kaplan turbines and the results have been validated against experimental data [62–64].

In the simulations, a fixed time step is consistently employed. The duration of the time step varies depending on the case and the fidelity of the CFD model

used in the different studies. The maximum runner rotation per time step at the nominal condition ranges between 0.17° and 2.25° in the simulations.

The convection term in Eq. (3.9) can be reformulated on a computational mesh to sum all fluxes on the surfaces of a computational cell as

$$\int_A (\phi \boldsymbol{u}) \cdot \boldsymbol{n} \, \mathrm{d}A = \sum_f (\phi \boldsymbol{u})_\mathrm{f} \cdot \boldsymbol{S}_\mathrm{f}, \tag{3.11}$$

where $\boldsymbol{S}_\mathrm{f}$ is the face area vector. In OpenFOAM, the volumetric face flux $(\boldsymbol{u} \cdot \boldsymbol{S})_\mathrm{f}$ is calculated and stored as a variable, here denoted $\Phi = (\boldsymbol{u} \cdot \boldsymbol{S})_\mathrm{f}$ [62]. However, the face value of the transported variable ϕ_f is determined by interpolation.

The convection term of the turbulent kinetic energy, the specific rate of dissipation and the liquid volume fraction (in Section 4.4 and Paper H) are managed with the first-order upwind scheme for stability reasons. With the first order upwind scheme, the face value ϕ_f is assumed to equal the cell centre value ϕ_c from the upwind cell [61].

The convection terms of the three velocity components are discretised with the LUST (linear-upwind stabilised transport) scheme [65]. The LUST scheme is a blend scheme that combines a central difference (CD) scheme for accuracy and a linear upwind (LU) scheme for stability. The LUST scheme is defined as

$$\phi_\mathrm{f,LUST} = \gamma \phi_\mathrm{f,LU} + (1 - \gamma) \phi_\mathrm{f,CD}, \tag{3.12}$$

where γ is a linear weight equal to 0.25 in OpenFOAM. Thus, LUST uses 25% of the linear upwind scheme

$$\phi_\mathrm{f,LU} = \phi_\mathrm{u} + (\boldsymbol{x}_\mathrm{f} - \boldsymbol{x}_\mathrm{u}) \nabla_\mathrm{u} \phi, \tag{3.13}$$

and 75% of the central difference scheme

$$\phi_\mathrm{f,CD} = \lambda \phi_\mathrm{u} + (1 - \lambda) \phi_\mathrm{d}, \quad \text{where} \quad \lambda = \frac{|\boldsymbol{x}_\mathrm{d} - \boldsymbol{x}_\mathrm{f}|}{|\boldsymbol{x}_\mathrm{d} - \boldsymbol{x}_\mathrm{u}|}. \tag{3.14}$$

The subscripts u and d are for upwind and downwind cell centres, respectively. The term $\nabla_\mathrm{u} \phi$ is the cell centre gradient at the upwind cell, and $\boldsymbol{x}$ is the spatial position of a cell or face centre.

Numerical schemes for diffusion are formulated similarly to the convection term as

$$\int_A (\Gamma \nabla \phi) \cdot \boldsymbol{n} \, \mathrm{d}A = \sum_f (\Gamma \nabla \phi)_\mathrm{f} \cdot \boldsymbol{S}_\mathrm{f}. \tag{3.15}$$

In the computations, the central difference scheme is used without any additional corrections for diffusion. The pressure gradient in Eq. (3.2) is a typical example of a source term. For all gradients, the central difference scheme is used without any corrections. Likewise, interpolation is managed with the central difference scheme.

3.1.3 Pressure-velocity coupling in OpenFOAM

For the unsteady computations in Papers A–G, the OpenFOAM `pimpleFoam` solver is used. The `pimpleFoam` solver is an incompressible solver that uses

the PIMPLE algorithm [66, 67] to establish a pressure-velocity coupling. The PIMPLE algorithm combines the SIMPLE [68] and the PISO [69] algorithms. Fig. 3.1 demonstrates the iterative solution procedure of the PIMPLE algorithm. PISO is used as an inner loop corrector step, and SIMPLE as an outer loop.

The OpenFOAM `interPhaseChangeDyMFoam` solver is used for the cavitating flow simulations in Paper H and Section 4.4. That solver also utilises the PIMPLE algorithm, with the addition that the liquid volume fraction is solved and corrected just before the momentum prediction within every SIMPLE loop.

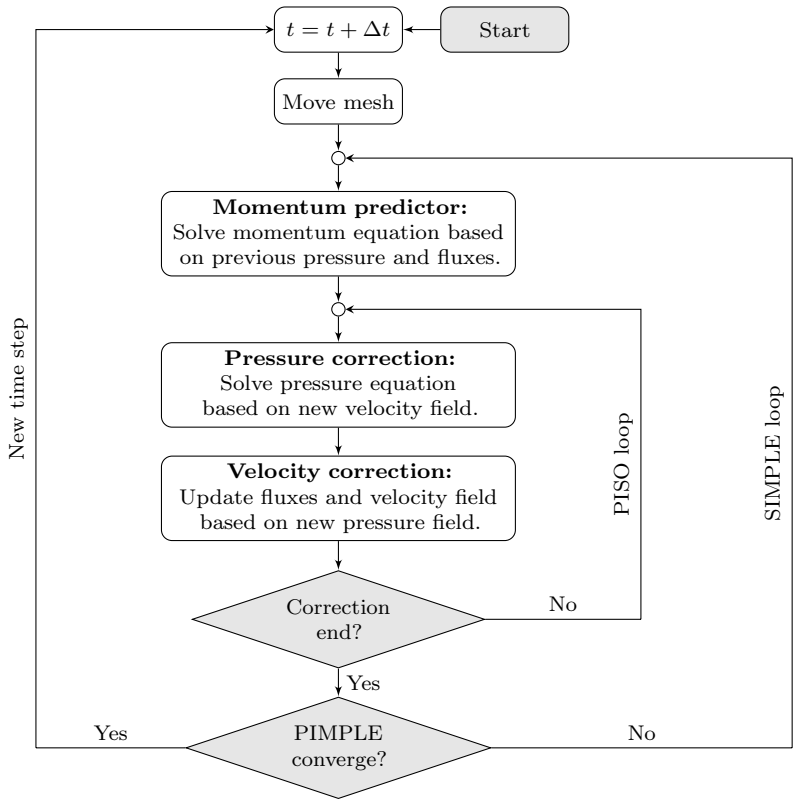

Figure 3.1: Flow chart of the PIMPLE algorithm [66, 67].

3.1.4 Steady-state simulation properties

Through the course of this PhD project, a countless number of steady-state simulations have been run. The purpose of these simulations has mainly been to provide data to various partners of the ALPHEUS project. The steady-state simulations are thus not the centre of this thesis. However, numerical and experimental results are compared in Section 4.5. Since the main goal of the experiments in the ALPHEUS project was to compare or validate steady-state conditions, most of the CFD results presented in Section 4.5 are based on steady-state simulations.

In the steady-state simulations, a sector model of the CRPT is used. The sector model contains one blade passage per runner, cyclic boundary conditions on the sides and a mixing-plane interface between the runners, as shown to the left in Fig. 3.2. The OpenFOAM `simpleFoam` solver is used for the steady-state simulations together with the multiple reference frame (MRF) [70] approach to model the rotating runners. In the steady-state rotating MRF approach with the absolute velocity in the rotating frame of reference (as implemented in OpenFOAM), the left-hand side of the momentum equation, Eq. (3.2), is re-written as

$$\frac{\partial \bar{w}_j \bar{u}_i}{\partial x_j} + \epsilon_{ijk} \Omega_j \bar{u}_k.$$

Here $\bar{w}$ is the relative velocity and Ω is the angular velocity applied to the rotating region. In the derivation of the MRF approach, centrifugal and Coriolis forces are considered.

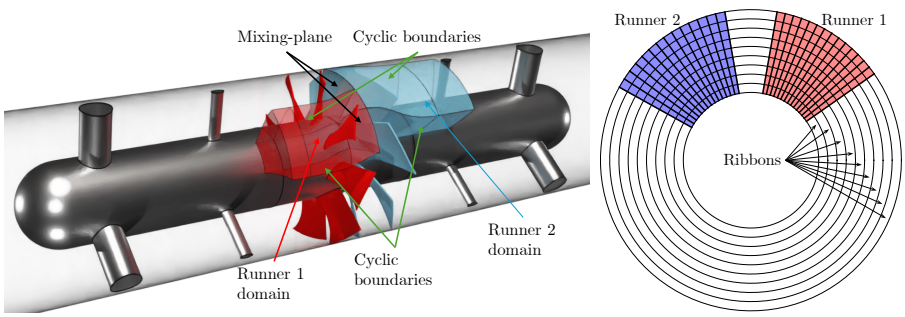

Figure 3.2: Illustration of steady-state domain (left) and principle view of mixing-plane (right).

The mixing-plane interface [71] is required between the runners since the number of blades differs for each runner. Specifically, Runner 1, with its eight blades, necessitates a 45° blade passage, while Runner 2, having seven blades, requires a 51° blade passage. The fundamental principle of the mixing-plane interface is illustrated to the right in Fig. 3.2. To transfer the flow variables from the non-overlapping Runner 1 and Runner 2 domains, the radial direction is divided into several circumferential ribbons. For each ribbon, the flow variables are averaged circumferentially and interpolated to the neighbouring patch. Moreover, by performing the circumferential averaging, the steady-state non-physical runner wakes between the rotating regions are mixed out.

3.2 System modelling

In any simulation, the outcome is invariably determined by the specified boundary conditions. Estimating appropriate boundary conditions is notoriously challenging without a deep understanding of the system or environment in which the studied component is situated. For a pump-turbine positioned within a penstock or conduit system, the flow rate depends on the energy extracted

or introduced by the pump-turbine and the hydraulic losses from all system components.

One option to achieve appropriate flow conditions is to include the entire hydraulic system in a full 3D CFD simulation. However, because of the substantial computational resources required for such a simulation, it is not a feasible alternative in most cases today [72]. Instead, the most common approach is to constrain the numerical domain to the component(s) of interest, which in the case of this thesis is the CRPT. This allows for the specification of static boundary conditions which are unaffected by the rest of the hydraulic system. This approach is used in Papers A, B and H. In Papers A and B it is used because no hydraulic system existed at that time, and in Paper H it is used since the machine is analysed without considering a specific hydraulic system.

An alternative strategy is to couple the space-constrained 3D CFD simulation with a 1D simulation representing the remainder of the system. In this approach, the flow rate and effects of the system components are balanced by the change of pressure across the computational domain. The method of characteristics (MOC) [73] and the method of implicit (MOI) [74] are two alternatives to accomplish this. Pressure waves are resolved in both MOC and MOI, which also requires pressure waves to be resolved in the CFD part. This imposes a significant constraint on the time step, thereby increasing the computational cost of the simulation because of the high speed of sound in water. To provide a more cost-effective approach to include the main effects from the components of the hydraulic system, which the CRPT is part of, the `headLossPressure` OpenFOAM boundary condition is developed in Paper C.

The basic principle of the `headLossPressure` boundary condition is that Bernoulli's energy equation [75] is applied to the boundaries of the computational domain to update and set the static pressure. For a boundary of the numerical domain, the pressure is calculated as

$$p_{\mathrm{P}} = p_{\mathrm{Far}} + \frac{\rho}{2}\left(u_{\mathrm{Far}}^2 - u_{\mathrm{P}}^2\right) + \rho g(z_{\mathrm{Far}} - z_{\mathrm{P}}) \pm \left(\Delta p_{\mathrm{l,Far}} + \Delta p_{\mathrm{f,Far}}\right). \tag{3.16}$$

Here u is the velocity, ρ is the fluid density, g is the gravitational acceleration, z is the location in the direction of the gravitational acceleration, Δp_{l} is pressure losses due to local occurrences in the flow path (local loss), and Δp_{f} is pressure losses caused by friction from the wall (friction loss). Subscript P is for patch (boundary), and 'Far' is a location up- or downstream in the hydraulic system. The losses are subtracted if 'Far' is located upstream (inflow boundary) and added if it is downstream (outflow boundary) of the computational domain.

The pressure losses because of local occurrences in the flow path, Δp_{l}, are caused by various sources such as valves, bends, instruments, etc. These losses can be characterised by a local loss coefficient for each of the system components. The local loss coefficients are typically found as tabulated values in textbooks, provided by the manufacturer, or estimated with numerical or experimental models. With the developed boundary condition in Paper C, it is further possible to specify a time-varying local loss coefficient, which for instance can be used to model a transient valve sequence.

The sum of pressure losses caused by wall friction, Δp_{f}, is calculated as a function of surface roughness, pipe length and hydraulic diameter, and a friction loss coefficient. The friction loss coefficient is solved iteratively through the Colebrook equation [75].

3.2.1 Experimental test facility

As a part of the ALPHEUS project, the model scale CRPT was experimentally tested by partners at TU Braunschweig by the end of 2023 and the first months of 2024 [76]. The initial plan of the ALPHEUS project was that the experimental tests would have taken place already in 2021. However, because of the worldwide supply chain issues resulting from the COVID-19 pandemic and the Suez Canal obstruction of March 2021, the tests were severely delayed. These delays lead to that in all appended papers, except Paper C, assumed characteristics have been used for the CRPT.

Figure 3.3 shows a 3D render of the experimental test facility at TU Braunschweig. It comprises two water tanks, lower and elevated, which are connected by pipes 1 and 2. The CRPT is situated in pipe 1, whereas pipe 2 is utilised during pump mode testing. In pump mode, water flows from the elevated tank via pipe 2 to the lower tank. In the lower tank, a spillway is present to maintain a relatively stable surface level and to get rid of the excess water that the CRPT cannot pump. The flow from pipe 2 must always exceed the pumped flow in pipe 1 to prevent the lower tank from draining. In turbine mode, water is released from the elevated tank to pipe 1 and through the CRPT. During turbine mode testing, pipe 2 is closed, and the water from pipe 1 flows

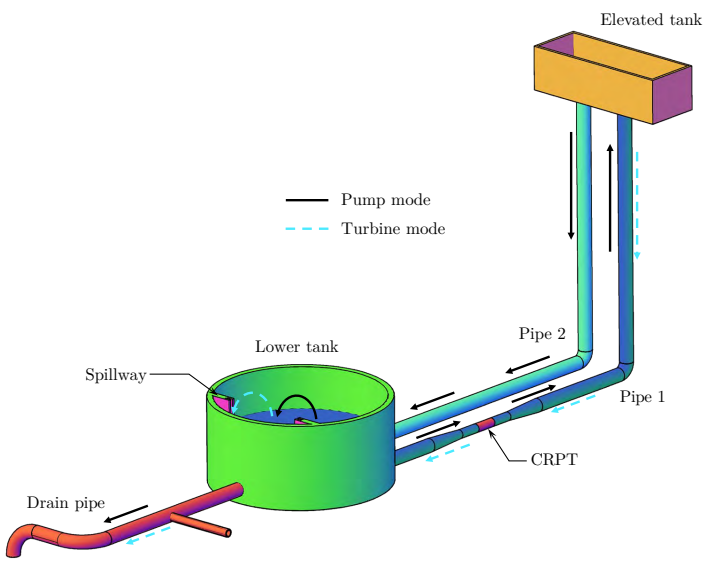

Figure 3.3: 3D render of the experimental test facility at TU Braunschweig (not to scale). Figure adapted with permission of Ruben Ansorena-Ruiz.

over the spillway into the drain pipe. The spillway height can be adjusted to achieve varying height differences between the lower and elevated tanks. Initially, the spillway was supposed to be adjustable to reach a difference in height elevations between 6.45 m to 8.45 m. However, during the construction of the test facility, the minimum possible elevation difference was revised from 6.45 m to 7.45 m.

Figure 3.4 depicts a schematic of the experimental test facility through pipe 1, with the numerical domain used in Papers F–H highlighted. In the studies where the `headLossPressure` is applied, the specified head losses are according to the schematic. However, the specified coefficients are based on textbook values or provided by the manufacturer of the components since no experimental data existed when conducting the studies. Table 3.1 shows a typical input when evaluating the machine in pump mode. The low-pressure and high-pressure labels are for the corresponding low- and high-pressure boundaries of the computational domain, respectively. The difference in surface elevations gives a gross head (H_g) of 7.45 m in this case. The local losses are according to White [75], except the 'Flow-control valve' which is based on provided data from the valve manufacturer. A loss coefficient for the flow meter is not specified since the manufacturer of the electromagnetic flow meter claims it has a negligible effect on the flow. The surface roughness provided for the friction losses is also based on White [75].

The local loss coefficient of the 'Flow-control valve' is characterised based on the earlier mentioned data from the manufacturer. The local loss coefficient of the valve, k_V, as a function of valve opening is approximated with an exponential function as

$$k_\mathrm{V}(\alpha_\mathrm{V}) = \exp(-4.2351 \ln(\alpha_\mathrm{V}) + 18.1149). \tag{3.17}$$

Here α_V is the valve opening in degrees. The exponential function in Eq. (3.17) is compared to the provided experimental test data of the valve in Fig. 3.5. Test data for the valve is only available between valve openings of 10°–90°, hence the smaller openings are extrapolated based on Eq. (3.17). It is reasonable to assume that the true local loss coefficient would follow the extrapolated values. This is because the local loss coefficient must approach infinity as the valve closes, and the curve fit shows an excellent agreement with the experimental data for the available opening angles. The value of k_V at 90° is 0.39, which is why this value is specified in Table 3.1 for the 'Flow-control valve'. In the simulations including a valve closure or opening, the smallest valve opening of 2° is used. The valve opening of 2° effectively prevents the flow in any direction while achieving a stable CFD simulation.

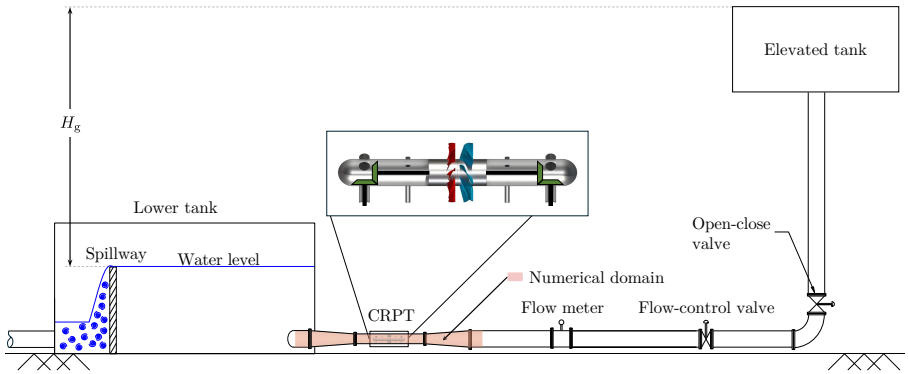

Figure 3.4: Schematic of the experimental test facility through pipe 1, see Fig. 3.3, at TU Braunschweig (not to scale). Figure adapted with permission of Ruben Ansorena-Ruiz.

Table 3.1: Typical input for the `headLossPressure` boundary condition at the low- and high-pressure boundaries at nominal operation of the CRPT.

	low-pressure	**high-pressure**	
Surface elevation	2.25	9.70	m
Local losses (loss coefficient)			
Bend	–	0.20	–
Sharp entrance	–	0.45	–
Sharp exit	1.00	–	–
Open-close valve	–	0.40	–
Flow-control valve	–	0.39	–
Friction losses			
Pipe length	1.00	15.05	m
Surface roughness	0.05	0.05	mm

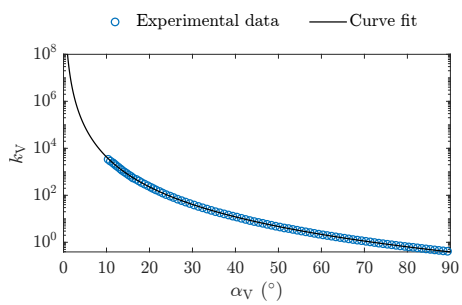

Figure 3.5: Local loss coefficient of the valve (k_V) as a function of valve opening (α_V), where 0° is fully closed and 90° is fully open.

Chapter 4

Selected results

The objectives of the CFD simulations have gradually evolved. Consequently, some general observations and results from preliminary studies of transients concerning the CRPT are first presented in Section 4.1, as well as in Papers A and B. The findings from these preliminary studies led to the realisation that the numerical framework needs to encompass a larger hydraulic system to predict a reasonable flow rate at any given operational point. The methodology employed to incorporate the effects of the hydraulic system in the CFD simulations is outlined in Section 3.2 and Paper C. Once the hydraulic system is modelled, the startup and shutdown sequences in pump mode are extensively analysed in Section 4.2 and Papers D–G. Corresponding transient operations in turbine mode are discussed in Section 4.3 and Paper G. In addition, cavitating flows at stationary conditions for the CRPT are presented in Section 4.4 and Paper H. Lastly, the results from the numerical simulations and experimental measurements are compared in Section 4.5 at stationary conditions.

4.1 General behaviour and preliminary transients

The CRPT produces complex flow patterns already at the design point, which is indicated by the vorticity magnitude in Fig. 4.1 and discussed in Paper A. This is primarily because the downstream runner interacts with the wakes of the upstream runner. The wake interactions of the runners lead to pressure oscillations correlated to the blade passing frequency of each runner, and various linear combinations of the two runners' blade passing frequencies. The blade passing frequency is defined as the number of runner revolutions per second times the number of runner blades.

During transient operations of the CRPT, such as a change of operational point or shutdown and startup procedures, the flow by the runners may undergo drastic changes. These changes can typically include flow separation by the runner blades, unbalanced torque distribution between the runners or flow in the reversed direction. All these phenomena may cause substantial runner

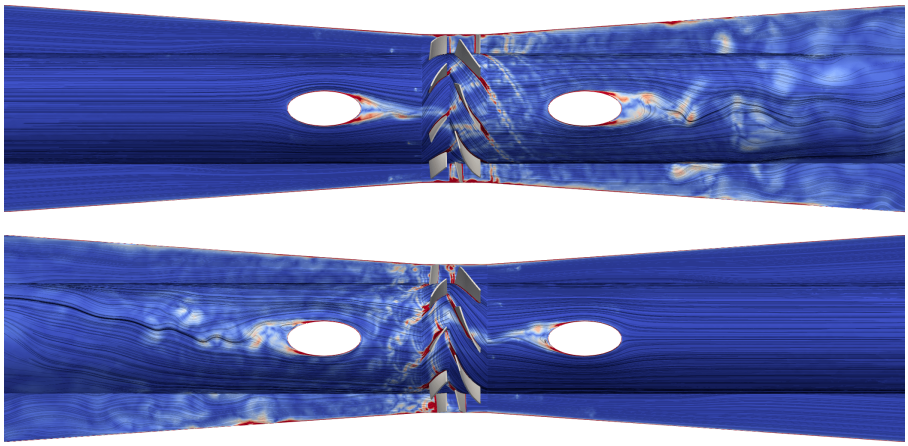

Figure 4.1: Snapshots of vorticity magnitude and streamlines of relative velocity displayed on a plane and a cylinder at the design point in pump mode (above) and turbine mode (below). Note that it is the above geometry in Fig. 2.3.

force and torque variations and peaks, which in turn can lead to fatigue or premature breakdown of the CRPT.

A large part of this thesis consists of the startup sequence in pump mode. In Paper B, it is shown that the runners exhibit fast and large load (force and torque) gradients and reversed flow during a preliminary startup sequence in pump mode. The pump mode shutdown sequence also indicated high amplitude load values and large load gradients. However, they are deemed not as severe as in the pump mode startup. Fortunately, the turbine mode loads are less substantial than in pump mode.

4.2 Startup and shutdown in pump mode

In Paper B, it is shown that using only the runners to control the pump mode startup sequence results in large force and torque gradients in the transition from the II brake quadrant into the I pump quadrant (see Fig. 2.5 for the RPT quadrants). A traditional startup sequence for PHS in pump mode typically includes the speedup of the runner to its nominal rotational speed with a closed valve or guide vanes [77]. Once the runner has reached its nominal speed and built up sufficient pressure, the valve or guide vanes are slowly opened up. A numerical simulation of such a sequence has been carried out while not included in the appended papers. In that simulation, the schematic hydraulic system shown in Fig. 3.4 is included, and a valve sequence is modelled with Eq. (3.17) through the `headLossPressure` boundary condition.

In Fig. 4.2, the computed flow rate, axial forces, and torques are shown for a traditional pump mode startup sequence. In the sequence, the rotational speed of the runners ($n_{\mathrm{R}i}$) are increased simultaneously from a standstill to the nominal rotational speed of 1502 rpm with the valve fully closed between

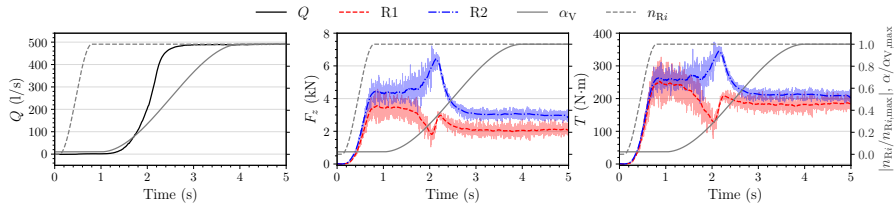

Figure 4.2: Flow rate (left), axial force (middle), and torque (right) as a function of time during the traditional pump mode startup sequence. In the normalised sequence on the right axis, a value of 0 is a closed valve (α_V), or no rotational speed (n_{Ri}), a value of 1 is an open valve and a rotational speed of 1502 rpm.

0.1 and 0.8 s. Subsequently during the sequence, the valve (α_V) is opened between 1 and 4 s. As the valve starts to open, the flow rate (left graph) rapidly increases. The flow rate is at 90% of its final flow rate already at 2.3 s, which is less than half the time of the transient valve opening sequence.

By analysing the axial forces (middle graph) and torques (right graph) of the two runners, it is shown that the general appearance is similar. At roughly 2.1 s, large peak values are noted for Runner 2 (downstream), while Runner 1 (upstream) indicates a drastic load decrease. After the peak at 2.1 s, the loads convert to their final values. The load fluctuations (indicated as shaded) are furthermore substantially larger before the peak at 2.1 s than after, for both runners. After the load peak, the load fluctuations on Runner 2 show smaller amplitude values compared to Runner 1.

One reason why Runner 2 experiences the most severe load conditions during the traditional startup sequence is because that runner encounters flow structures leaving the upstream Runner 1. This is evident from the vorticity magnitude in Fig. 4.3 at 2.1 s and 3.5 s. At the earlier time step, the flow field is heavily separated by both runners, whereas it is more attached at the later time step. With the traditional sequence, it is clear that there is a tipping point before and after around 2.1 s. A physical explanation of what is happening is that, as the flow rate increases whilst opening the valve, the flow is swirled in the direction of Runner 1's rotation between the runners. However, the swirl is in the opposite direction downstream of Runner 2 because of that runner's rotational direction. The drastic change of swirl direction over Runner 2, combined with the rapid acceleration in flow rate and heavily separated flow field from Runner 1 (compare 2.1 s and 3.5 s in Fig. 4.3) causes the high Runner 2 loads at around 2.1 s. As the flow rate continues to reach its final value, the swirl between the runners decreases due to the increasing flow rate. Moreover, once the machine reaches its final operating condition, the upstream flow field of Runner 2 is less separated since the flow is appropriately guided through the blade passages of Runner 1, as demonstrated in Fig. 4.3.

Because the traditional sequence does not yield any more promising results than those presented in Paper B, the studies in Paper D and Paper E were carried out. In Paper D, the physical time of the startup sequence is evaluated,

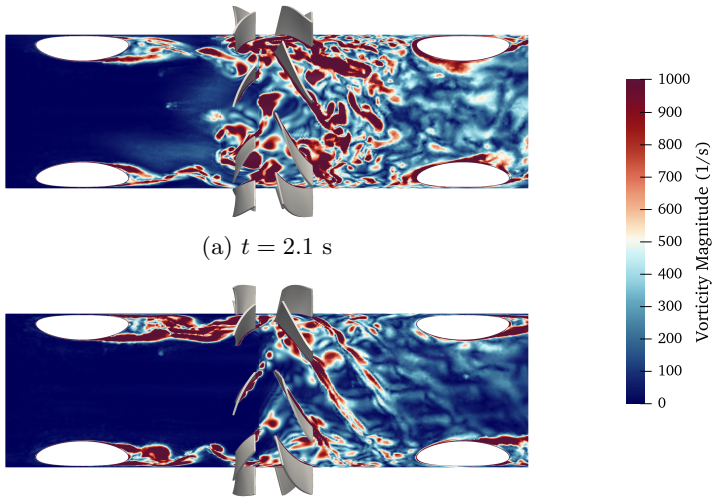

(a) $t = 2.1$ s

(b) $t = 3.5$ s

Figure 4.3: Snapshots of vorticity magnitude on a cylinder by the runners at two time steps during the traditional pump mode startup sequence. The flow is from left to right, and it is the middle geometry in Fig. 2.3.

whereas in Paper E the startup sequence is optimised while using the shortest time from Paper D. The primary goal of both studies is to identify viable alternatives for starting up the CRPT in pump mode and avoiding such high-amplitude loads as demonstrated in Fig. 4.2 and Paper B.

Although the pump mode shutdown in Paper B is considered less severe than the equivalent startup procedure, the pump mode shutdown sequence is assessed in Paper F. In that study, it is investigated whether it is preferable to close a valve before or after speeding down the runners. The latter option is, in principle, the sequence evaluated in Paper B. It is found that from a peak load point of view, it is favourable to close the valve before speeding down the runners. On the other hand, the load fluctuations increase by closing the valve before speeding down the runners.

In an effort to improve the pump mode shutdown sequence further, that sequence is investigated to find a trade-off between the experienced peak loads and the amplitude of the load fluctuations. Fig. 4.4 shows a selection of the evaluated pump mode shutdown sequences. Case I is the preferred sequence from Paper F. However with differences in the nominal conditions, as explained in Section 4.2.1, and using linear functions to control the sequences instead of sinusoidal ones. Cases II and III use slightly faster valve closure than case I, and the runners are brought to a standstill at an earlier stage. The difference between cases II and III is that in the latter, Runner 1 speeds down shortly after Runner 2.

The change in flow rate during the pump shutdown, as shown in the middle of Fig. 4.4, is fairly consistent with the cases. The main reduction in flow rate

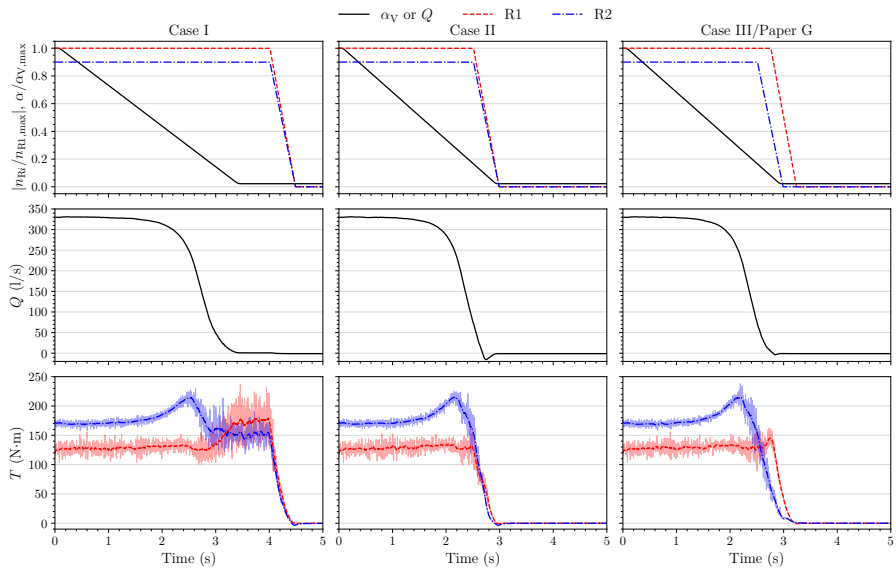

Figure 4.4: Pump mode shutdown cases, above sequence, middle flow rate, and below torque as a function of time. Note, simulations made with LoFi CFD model from Paper E.

occurs as the valve approaches the fully closed state. In case II a small amount of reversed flow is noted because the CRPT net head cannot overcome the gross head as the runners are brought to a standstill. Reversed flow is effectively avoided in the other sequences.

Focusing on the torque, below in Fig. 4.4, it is discovered that the peak torque value on Runner 2 is practically the same in all cases. The Runner 1 torque presents more significant differences compared to the Runner 2 torque. In case I, the Runner 1 torque shows the largest peak values and fluctuations (indicated as shaded). Both cases II and III present much smaller torque fluctuations since the runners are brought to a standstill as the flow rate diminishes. Because cases II and III exhibit similar behaviour in the torque during the sequences, case III is selected for Paper G. The main reason for this is that reversed flow is avoided. Additionally, case II indicates a small negative torque for Runner 2 as the flow rate is in the reverse direction.

4.2.1 Change of nominal conditions in Paper G

In Paper G, the nominal pump mode operating conditions from Papers D–F are modified because of updates made during the lab construction. First of all, the planned maximum spillway height in the lower tank (see Fig. 3.4) had to be decreased by 1 m. Consequently, the minimum gross head increased from 6.45 m to 7.45 m. Furthermore, preliminary studies of cavitating flows (see Section 4.4 for example) indicated a need to change the rotational speed of the

runners to reduce the risk of cavitation.

The modifications in gross head and reduced rotational speeds in Paper G, compared to Paper E, caused the nominal operating conditions of the pump mode to shift towards the hump zone. This shift is illustrated by the Q_{11}-n_{11} curve in Fig. 4.5. As a result, the peak loads and load gradients on Runner 2 increase during the pump mode startup sequence. This increase is presumed to occur because the hump zone is passed at a later stage in the sequence compared to the sequence outlined in Paper E.

Because of the larger gross head used in Paper G, the runner rotational speeds needed to be increased from those used in Paper F to start up the machine in pump mode. This increase in gross head and rotational speeds led to the larger runner loads experienced during the pump mode shutdown in Paper G compared to Paper F. It should be noted that the rotational speeds used in Paper F (see P_2 in Table 4.1) were selected based on minimising the risk of cavitation. As a consequence, the CRPT is working on the verge of the hump zone at the nominal operating condition in Paper F. This explains why the rotational speeds used in Paper F can not be used in Paper G because of the larger gross head.

In Fig. 4.5, it can be observed that the estimated shape of the hump zone is significantly influenced by whether steady-state or unsteady simulations are employed. The hump zone appears exaggerated in the simplified steady-state approach compared to the more realistic unsteady simulation approach. The flow field within the hump zone is characterised by unsteady flow structures and large fluctuations, which cannot be captured by a steady-state model. Apart from the hump zone, the characteristics of the pump mode operation remain consistent, regardless of whether the steady-state or unsteady simulation approach is used.

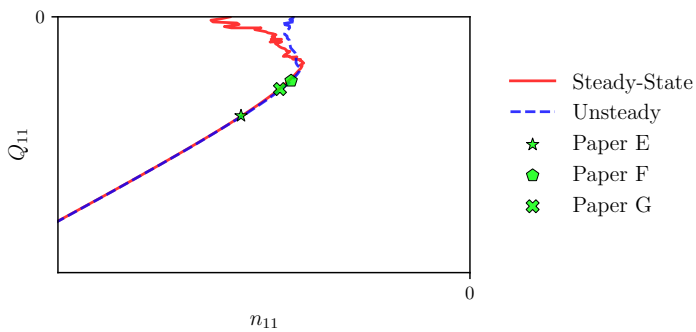

Figure 4.5: Characteristics of Q_{11}-n_{11} (see Eqs. (2.4) and (2.5)) in pump mode using steady-state simulations on a sector model (see Section 3.1.4), and unsteady simulations on a full 360° domain, as well as the nominal operating conditions for Papers E–G marked.

4.3 Startup and shutdown in turbine mode

Several startup and shutdown sequences in turbine mode have been evaluated with the aim of avoiding negative torque (turbine brake) and limiting load gradients. To compare the sequences, the objective function from Paper E is evaluated,

$$f = \int \left(\left| \frac{\partial \bar{F}_{z,\mathrm{R1}}}{\partial t} \right| + \left| \frac{\partial \bar{F}_{z,\mathrm{R2}}}{\partial t} \right| \right) \mathrm{d}t. \tag{4.1}$$

Here $\bar{F}_{z,\mathrm{R1}}$ and $\bar{F}_{z,\mathrm{R2}}$ are the instantaneous average axial force for Runner 1 and 2, respectively, in kN.

Above in Fig. 4.6 shows a selection of the evaluated turbine mode startup sequences, culminating in the sequence outlined in Paper G. For all turbine mode startup sequences, the valve starts to open before starting to speed up the runners. The reason for this is that a sufficient flow needs to be developed to avoid negative torque, which is achieved in all sequences.

The main difference in the displayed startup sequences is when and how to initiate the speeding up of the runners. Case A has a later start-to-speed-up time, indicating a later initiation, while cases B and C have an earlier, indicating a sooner initiation. The difference between cases B and C is that in the latter, the runners speed up simultaneously. The start-to-speed-up time quite affects the time evolution of the flow rate. In case A, the flow rate (middle in Fig. 4.6) settles at around 150 l/s before speeding up the runners. In the other cases, the flow rate does not have time to settle as the runners start guiding the flow

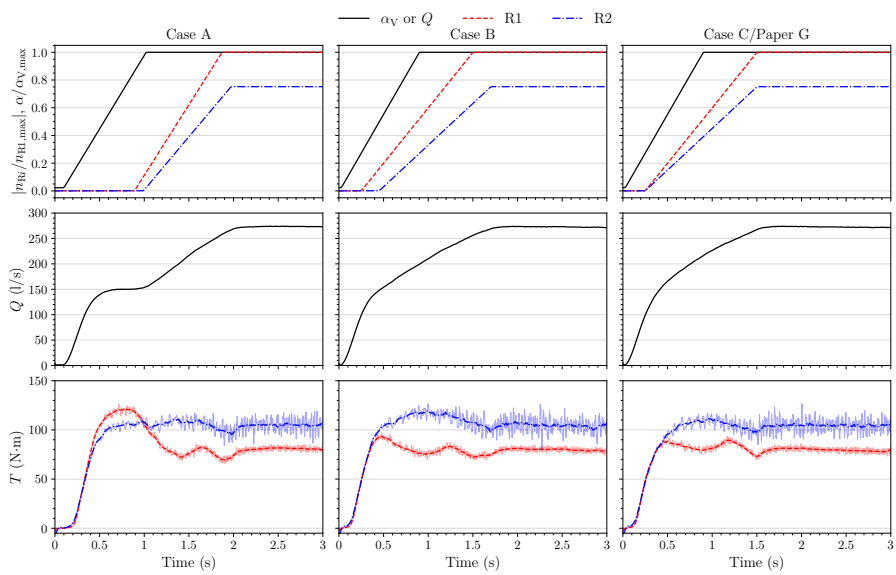

Figure 4.6: Turbine mode startup cases, above sequence, middle flow rate, and below torque as a function of time. Note, simulations made with LoFi CFD model from Paper E.

in the blade passages during the valve opening.

Focusing on the runners' torque during the startup sequences, below in Fig. 4.6, it is found that Runner 1 is more sensitive than Runner 2. In case A, the largest Runner 1 torque is noted. The peak torque occurs as the flow rate settles, and the runners simply block the flow as they are at a standstill. In case B the Runner 1 torque peak at around 0.5 s is drastically reduced, and in case C it is barely reconcilable. This indicates that it is favourable to start speeding up the runners earlier to reduce the Runner 1 peak torque value. The Runner 2 peak torque is the largest in case B. Fortunately, when speeding up the runners simultaneously in case C, the Runner 2 peak torque value is reduced. By computing the objective function in Eq. (4.1) it is confirmed that case C is the preferred option, which is the reason why it is selected for the mode-switching studies in Paper G. The objective function is 4.79, 4.10 and 3.64 kg·m/s^2 for cases A, B and C, respectively.

A number of turbine mode shutdown sequences have been evaluated, and in Fig. 4.7 a small selection is shown leading to the sequence presented in Paper G. Above in the figure the evaluated sequences are shown. The basic principle of the sequences is that the valve starts closing at the initial time step to reduce the flow rate before speeding down the runners. The multi-stage valve closure is proposed to reduce the runner loads while reducing the rotational speeds. In case D, the first part of the valve closure is longer compared to case E, while the time at the plateau is shorter in case D. The second part of the valve closure is similar for all cases, however it is slightly longer in case D. The valve closure

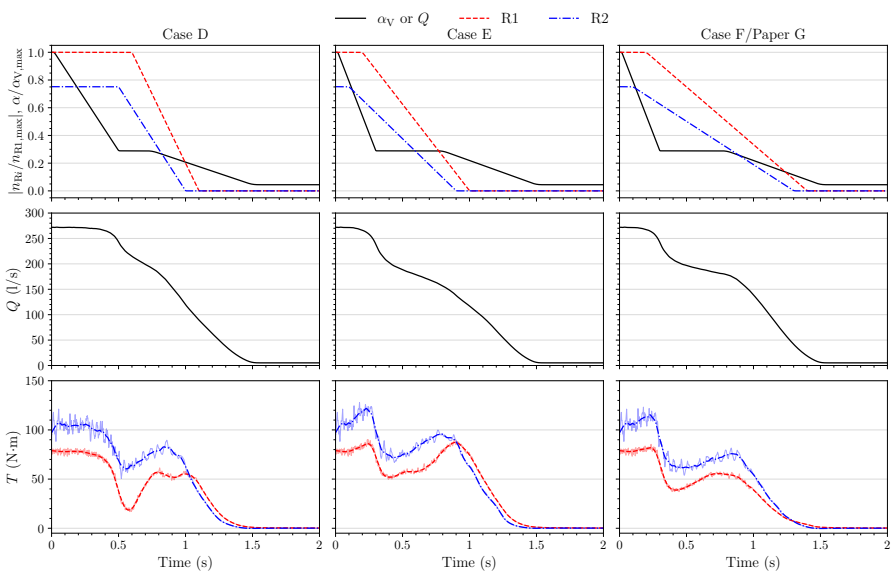

Figure 4.7: Turbine mode shutdown cases, above sequence, middle flow rate, and below torque as a function of time. Note, simulations made with LoFi CFD model from Paper E.

in cases E and F are equivalent. Case D utilises the shortest speed-down-time of the runners and case F the longest.

Because of the longer first part of the valve closure in case D, the initial reduction in flow rate is delayed compared to the other cases. As the flow rate reduces in case D, the torque on the runners drops drastically. When the valve closure plateau at 0.5 s is reached, Runner 2 starts to speed down, shortly followed by Runner 1. The torque is initially further reduced, however, at 0.57 s the torque increases rapidly because of the decelerating runners. In the other cases, while larger peak values are exhibited, the positive Runner 1 torque gradient is reduced when either case E or case F sequences are employed.

The difference between cases E and F is that in the latter, the speed down of the runners is longer. By using the longer speed-down-time, the torque gradients are reduced and thus deemed as a preferable alternative. By computing the objective function from Paper E, Eq. (4.1), it is furthermore confirmed that case F is the favourable option. The objective function is 3.95, 4.92 and 3.69 kg·m/s^2 in cases D, E and F, respectively, which is why case F is used in Paper G.

4.4 Cavitating flow simulations

In a preliminary study designed to support the experimental tests of the CRPT in the ALPHEUS project at TU Braunschweig, cavitating flows were examined for the CRPT. Four operating conditions are investigated using non-cavitating and cavitating flow simulations. These four operating conditions, displayed in Table 4.1, represented the anticipated extreme conditions in the test facility at that time. Two cases are evaluated in each mode, with the cases marked with index 1 representing the case most likely to experience cavitation. In pump mode, two sets of runner rotational speeds are evaluated, with case P_2 utilising the lower set of rotational speeds. In contrast, in turbine mode, the rotational speed of the runners is the same in T_1 and T_2. Instead, two different gross heads are evaluated in turbine mode. The gross head in T_1 represents the lowest possible spillway height, whereas in T_2 and the pump mode cases, the anticipated highest spillway is used. The word 'anticipated' is used because it was later discovered during the construction of the test facility that the initially planned highest spillway could not be achieved. The `headLossPressure` boundary condition developed in Paper C is applied in these simulations to obtain realistic absolute pressures, which is crucial for

Table 4.1: Operating conditions for the cavitating flow simulations.

	Pump P_1	Pump P_2	Turbine T_1	Turbine T_2	
Gross head (H_g)	6.45	6.45	8.45	6.45	m
Runner 1 speed (n_{R1})	1502	1129	842	842	rpm
Runner 2 speed (n_{R2})	1129	849	633	633	rpm

cavitating flows as the phase change depends on the absolute pressure.

The computed engineering quantities, see Eqs. (2.1)–(2.3), at the two turbine mode operating conditions are presented in Table 4.2. A comparison of the results from the non-cavitating ($\sigma = \infty$) and cavitating ($\sigma \neq \infty$) flow simulations shows that the engineering quantities are similar. The maximum deviation is just above 1% and occurs for the computed power of T_2. The small difference between the results of the cavitating and non-cavitating flow simulations is plausibly explained by the relatively large σ values (see Eq. (2.6)) in both operating conditions. To determine the amount of cavitation at the evaluated operating conditions, the liquid volume fraction, α_l, can be further investigated.

Figure 4.8 shows iso-surfaces of the liquid volume fraction to indicate cavitating regions at the two operating conditions. For T_1, there is a clear region with cavitation at the leading edge of the low-pressure Runner 1. The cavitation is at this location caused by a low pressure zone originating from leading edge flow separation at the suction side of the runner blade surface. At T_2, there are no visible regions of cavitating flow. On the high-pressure Runner 2, no traces of cavitation are indicated in any of the operating points. The small amount of cavitation indicated at T_1 has a negligible effect on the

Table 4.2: Time-averaged engineering quantities in turbine mode for non-cavitating ($\sigma = \infty$) and cavitating ($\sigma \neq \infty$) flow simulations.

	P (kW)	Q (m^3/s)	H (m)	η_T (%)
T_1, $\sigma = \infty$	16.92	0.29	6.76	89.46
T_1, $\sigma = 1.71$	17.06	0.29	6.80	89.55
Difference (%)	0.82	0.00	0.59	0.10
T_2, $\sigma = \infty$	11.48	0.26	5.03	89.62
T_2, $\sigma = 2.69$	11.62	0.26	5.06	89.87
Difference (%)	1.22	0	0.60	0.28

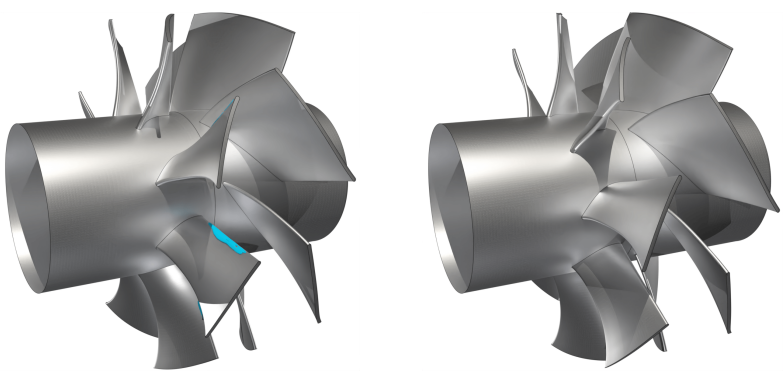

Figure 4.8: Snapshots of liquid volume fraction iso-surface $\alpha_l = 0.9$ in turbine mode, T_1 to the left and T_2 to the right.

machine performance, as seen in Table 4.2.

The computed engineering quantities of the two pump mode operating conditions are presented in Table 4.3. Larger differences between non-cavitating and cavitating flow conditions are seen for P_1 than for P_2. For the cavitating P_1 case ($\sigma \neq \infty$), the power is for instance over-predicted, while both the flow rate and head are under-predicted compared to the non-cavitating case ($\sigma = \infty$). The effects of this are seen in the computed efficiency, presenting a worse result for the cavitating case. In P_2 however, the results are marginally different between the cavitating and non-cavitating flow simulations.

A reason why P_1 performs poorly when cavitation is considered is found by investigating the cavitating regions in Fig. 4.9. It is seen that a non-uniform cavitating region covers a large part of the Runner 1 blades' suction side, where some blades are almost completely covered by cavitation. For P_2, comparably smaller parts at the leading edges of Runner 1 experience cavitation. This large difference in cavitating regions can explain the significant variation in the machine performance when cavitation is considered and when it is not for P_1 and P_2.

This preliminary investigation shows that cavitation can be expected during the experimental tests at TU Braunschweig for some operating conditions. It

Table 4.3: Time-averaged engineering quantities in pump mode for non-cavitating ($\sigma = \infty$) and cavitating ($\sigma \neq \infty$) flow simulations.

	P (kW)	Q (m^3/s)	H (m)	η_P (%)
P_1, $\sigma = \infty$	48.79	0.42	10.10	85.77
P_1, $\sigma = 1.36$	49.33	0.41	9.84	79.58
Difference (%)	1.11	2.38	2.57	7.22
P_2, $\sigma = \infty$	23.82	0.27	7.89	86.93
P_2, $\sigma = 1.70$	23.93	0.27	7.87	86.06
Difference (%)	0.46	0	0.25	1.00

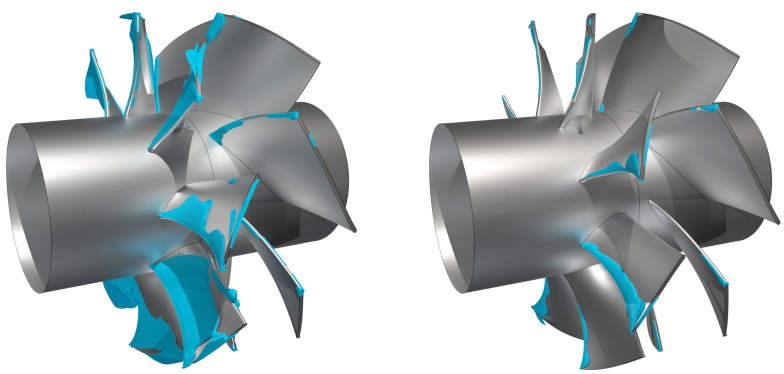

Figure 4.9: Snapshots of liquid volume fraction iso-surface $\alpha_l = 0.9$ in pump mode, P_1 to the left and P_2 to the right.

is further demonstrated that cavitating flows have an impact on the machine's performance. The findings from this preliminary study of cavitating flows for the CRPT led to the work presented in Paper H. The aim of the study in Paper H is to understand how and why cavitation affects the performance of the CRPT.

4.5 Comparison of numerical and experimental data

Experimental measurements of the CRPT were carried out as part of the ALPHEUS project. However, because of the previously mentioned severe delays of the measurements, no conclusive validation of the CFD results could be made within this thesis. In this section, a selection of experimental and numerical results are compared. The goal is to highlight potential differences in measurements and numerical simulations which may partly explain the deviations in results. Moreover, most of the CFD results are based on steady-state simulations for a single blade passage, as explained in Section 3.1.4.

In the comparison of experimental and numerical results, numerical results are presented using various solver properties. Therefore, to aid the reader, the following paragraph provides a brief description of the labels used in the graphs in this section. First of all, the experiments are denoted as 'Experiments'. Simulations using the `headLossPressure` boundary condition are denoted as '`headLossPressure`'. Note however that the loss coefficients used in the `headLossPressure` boundary condition are not calibrated based on the experimental data. For all other numerical simulations, the flow rate is specified based on the measurements. Moreover, this section evaluates several linear eddy-viscosity turbulence models. The one-equation Spalart-Allmaras model [78] is denoted as 'SA'. The standard k-ω two-equation model [79] is denoted by 'k-ω'. The SST [55] variant of the k-ω model is denoted as 'k-ω SST'. The two-equation k-ε realizable model [80] is denoted by 'k-ε realizable'. The simulations that utilise the foam-extend 4.1 nextRelease (revision 2d9985) variant of OpenFOAM, with the k-ω SST turbulence model, is denoted as 'fe4.1NR, k-ω SST'. Note that the other steady-state simulations are made using OpenFOAM v2306. Unsteady simulations have been employed on a few cases and are denoted as 'k-ω SST-SAS' since that turbulence model is used for the unsteady simulations. Note that in the `headLossPressure` simulations, the k-ω SST turbulence model is used.

Because the test facility consists of two open water surfaces, the rotational speed of the runners is varied to test the machine at different flow rates during the experiments. In the CFD simulations, the rotational speeds from the experiments are imposed. The rotational speed ratio, used in the graphs through this section, is defined as

$$\mathrm{r} = \frac{n_{\mathrm{R2}}}{n_{\mathrm{R1}}}. \tag{4.2}$$

4.5.1 Comparison in pump mode

Figure 4.10 shows a comparison in pump mode of experimental and numerical results using the different solver properties at the 0.9 runner speed ratio. At first glance, the CFD simulations using the `headLossPressure` boundary condition seem to present the results which are the closest to the experiments. However, with the assumed losses used when setting up the boundary condition, the full flow rate range cannot be covered, meaning there is a mismatch in the flow rate and specified runner rotational speeds.

By assessing the steady-state simulations using different turbulence models, the results with the standard k-ω model display a behaviour not seen with the other tested models. The prediction of the head (above left) is significantly underestimated, and the power (above right) has a different slope in the results from the k-ω model compared to the results from the other turbulence models. This leads to a completely different appearance in efficiency (below left) with the k-ω model. The remaining steady-state results indicate a similar prediction of the head and power regardless of which model is employed. In the experiments, a monotonic increasing trend is noted for the head. None of the steady-state CFD results is able to reproduce the slope from the experiments. On the other hand, the steady-state simulations almost reproduce the slope of the power, albeit with an offset. The steady-state simulations recognise the initial increase in efficiency with an increasing flow rate. However, the peak efficiency at the higher flow rates is offset.

Out of the evaluated steady-state cases in pump mode, the 'fe4.1NR, k-ω SST' results are, on average, closest to the measurements. This is shortly

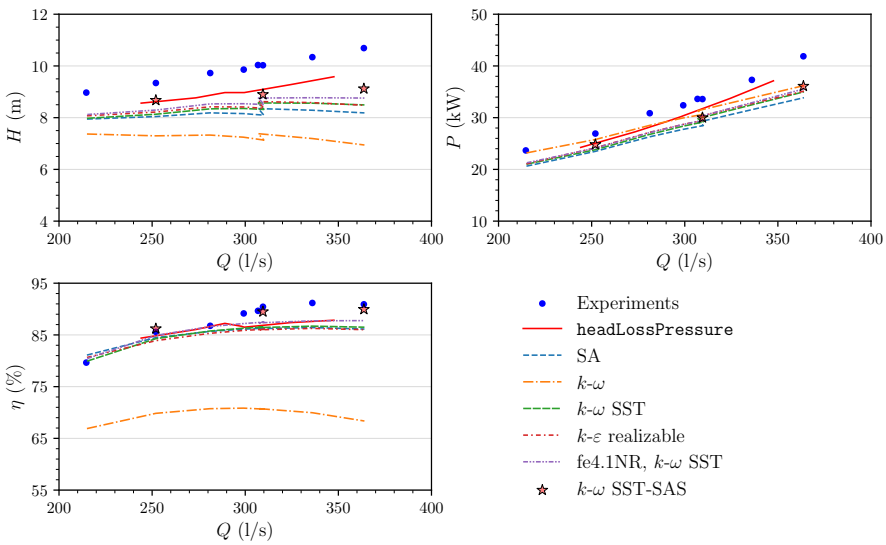

Figure 4.10: Pump mode at r = 0.9, with experimental and numerical results using different solver properties.

followed by the 'k-ω SST' and 'k-ε realizable' results. By using any of these three models, the average difference between CFD and measurements for the head, power, and efficiency is around 15%, 12%, and 3%, respectively. Hence, none of the steady-state results can reproduce the measurements precisely. This may be because the flow field is not steady, and thus a steady-state simulation cannot capture the flow accurately. For that reason, three unsteady simulations using a full 360° domain and rotating runners are evaluated. By using the unsteady simulations, denoted as 'k-ω SST-SAS', the head and power predictions marginally improve. There is however still a clear difference between CFD and measurements for the predicted head and power. On the other hand, the efficiency is almost spot on, suggesting that the relationship between head and power remains consistent between unsteady simulations and measurements in pump mode.

In the next phase, steady-state pump mode results are compared at different runner speed ratios in Fig. 4.11. Unfortunately, this comparison of a wider operating range leads to similar conclusions as when comparing results using different solver properties in Fig. 4.10. Namely, the head is completely different between experimental and numerical results. Also, the slope of the power is flatter in the CFD compared to the measurements. These discrepancies in the behaviour of the CRPT may indicate that some different physical phenomena are occurring in the experiments and the CFD simulations.

In the CFD simulations, the flow rate and runner rotational speeds from the measurements are imposed as boundary conditions. The flow rate is for

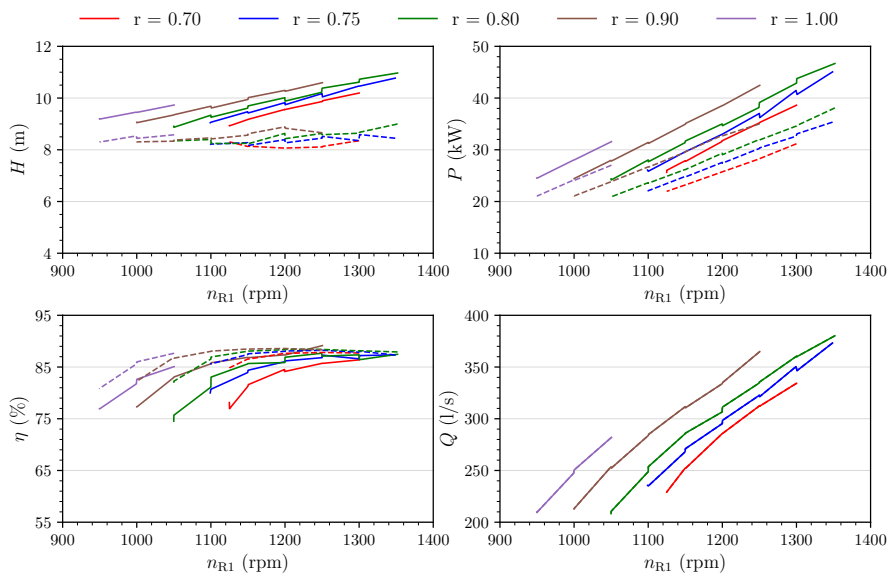

Figure 4.11: Pump mode, experimental and numerical results at different runner speed ratios (r). Experiments are solid lines, and the CFD are dashed. The below right graph shows the evaluated operating and boundary conditions.

instance typically difficult to measure accurately. Further, a uniform inflow is assumed in the CFD simulations. The assumption of a purely axial inflow condition cannot be verified in the experiments. Because the CRPT is designed for an axial inflow, even a small incoming tangential velocity can potentially have a large impact on the CRPT's performance.

To evaluate how the performance of the CRPT is influenced by incoming tangential velocity, Fig. 4.12 shows the engineering quantities as a function of the ratio of incoming tangential velocity to axial velocity. In this figure, a fixed flow rate and rotational speed of the runners are considered. The incoming tangential velocity largely affects the head and power, and hence the efficiency. By using a positive tangential velocity, the head and power decreases with the increase in tangential velocity. The efficiency is on the other hand comparably stable. By using a negative tangential velocity, the head and power increase up to $u_\theta/u_z \approx -0.4$, whereafter they rapidly reduce with a larger negative tangential velocity. As the head and power are reduced, the efficiency is likewise decreased. The difference between the measured and numerically predicted efficiency is the smallest at around $u_\theta/u_z = -0.32$. This indicates that it is possible that the flow in the experiments is not purely axial, which was previously assumed.

To illustrate what effect the incoming tangential velocity has on a larger operating range of the CRPT, Fig. 4.13 shows the operating performance at $u_\theta/u_z = -0.32$ at different runner speed ratios. Note that Fig. 4.13 is the same comparison as in Fig. 4.11, with the difference that in the CFD simulations, the tangential velocity is set as $-0.32u_z$. By assuming the negative tangential velocity, the trends of the head and power indicate better agreement between measurements and CFD. This strengthens the hypothesis that the flow may not be purely axial in the experiments. Additional potential reasons for the difference between measurements and CFD are further discussed in Section 4.5.3.

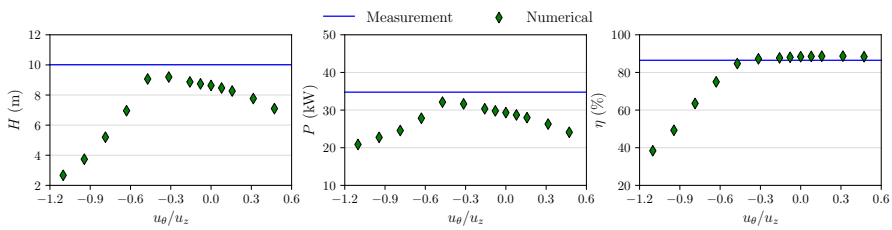

Figure 4.12: Pump mode, engineering quantities as a function of the incoming tangential velocity divided by the axial velocity at $Q = 307$ l/s ($u_z = 6.4$ m/s), $n_{\mathrm{R1}} = 1200$ rpm and r = 0.80.

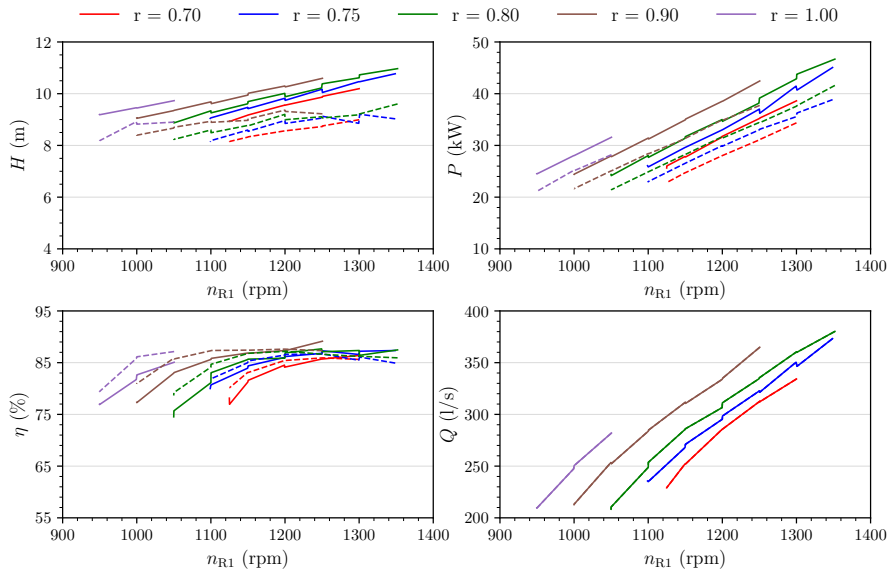

Figure 4.13: Pump mode, experimental and numerical results at different runner speed ratios (r), with $u_\theta/u_z = -0.32$. Experiments are solid lines, and the CFD are dashed. The below right graph shows the evaluated operating and boundary conditions.

4.5.2 Comparison in turbine mode

Figure 4.14 compares the computed engineering quantities in turbine mode between experimental and numerical results using different solver properties in the CFD simulations. Because the standard k-ω model presented deviant results in pump mode, it is neglected from the turbine mode comparison. The `headLossPressure` results show the largest deviations from the experiments at the lower flow rates, whereas the nearest match at the higher flow rates. The other steady-state results present a large spread in the predicted head at flow rates below 250 l/s. The power is on the contrary practically identical between CFD and experiments regardless of turbulence models below about 270 l/s. At flow rates above 270 l/s, the head has an adequate agreement, whereas the power from the CFD simulations is larger compared to the experiments. Overall, the efficiency computed with CFD is slightly overestimated. Employing the unsteady 'k-ω SST-SAS' simulations, with the full 360° domain and rotating runners, does not improve the agreement at the higher flow rates.

The predicted head and efficiency are, on average, closest to the experimental data using the 'k-ω SST' or the 'fe4.1NR, k-ω SST' options. The average difference between CFD and measurements using any of these alternatives is around 4%, 6%, and 10% for head, power, and efficiency, respectively. The results using the 'SA' model present a 2% difference for the power, whereas the head and efficiency indicate larger discrepancies compared to any of the

k-ω SST options.

In Fig. 4.15, a comparison of a large operating range using different runner speed ratios (r) in turbine mode is shown. The head aligns with the measurements at rpm below 800. At the higher rpm, the head is larger in the CFD simulations compared to the experiments. The power is, just like the head, similar for rpm below 800. At the higher rpm, the power is larger in the CFD simulations compared to the measurements. The effect of this on the efficiency is that the CFD simulations have a higher estimated efficiency. However, the shape of all engineering quantities is similar between simulations and experiments.

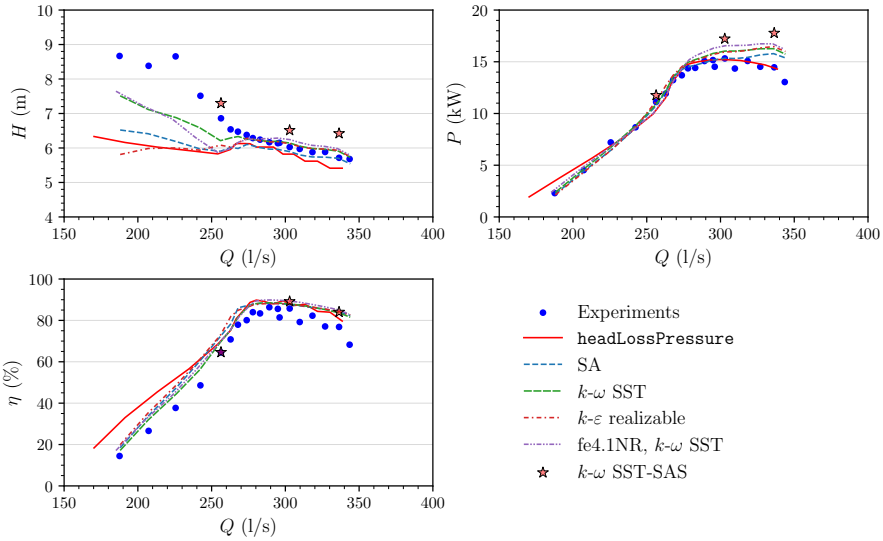

Figure 4.14: Turbine mode at r = 0.9, with experimental and numerical results using different solver properties.

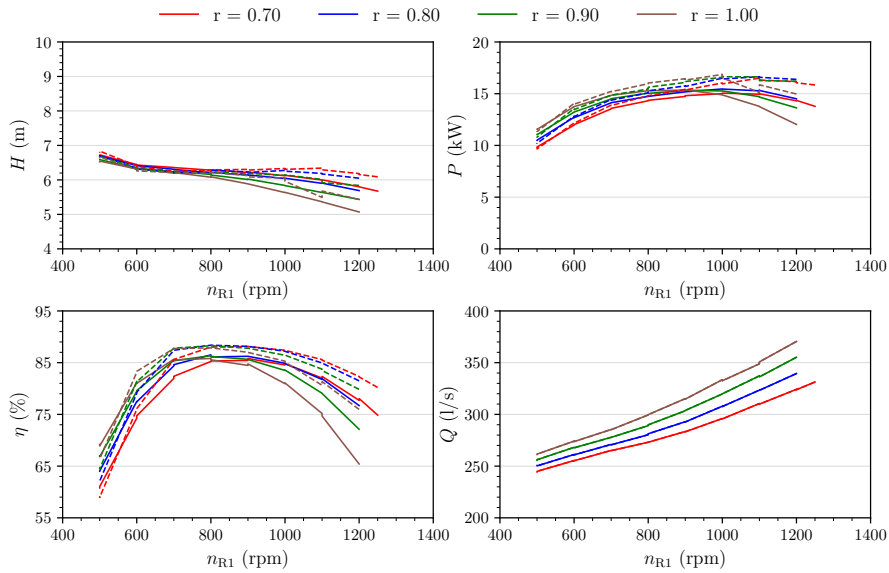

Figure 4.15: Turbine mode, experimental and numerical results at different runner speed ratios (r). Experiments are solid lines, and the CFD are dashed. The below right graph shows the evaluated operating and boundary conditions.

4.5.3 Potential sources for discrepancies

Several factors and potential uncertainties contribute to the discrepancy between the results of the CFD simulations and the experimental measurements. In this study, different solver properties are evaluated in the steady-state CFD simulations. The general appearance of the CFD results is marginally affected by the choice of turbulence model, with the exception of the standard k-ω model. This suggests that the choice of turbulence model may be less critical and that other factors could play a more significant role. Firstly, the steady-state CFD simulations are carried out for a single blade passage of each runner. In such an approach, the flow is assumed to be symmetric for all runner blades. Secondly, the inlet and outlet boundaries in the steady-state simulations are positioned very close to the runners. In the CFD simulations, constant values are applied as boundary conditions, whereas the flow properties may be far from constant near to the runners. This is particularly true at off-design conditions where the flow can be largely separated. Thirdly, the mounting arrangement is not considered in the steady-state simulations. The separated flow from the support struts influences the incoming flow towards the runners, thereby plausibly impacting the performance of the machine.

Experimental measurement campaigns inherently present various sources of uncertainties and errors. These errors may arise from factors such as instrument accuracy, systematic errors, or human error. At the time of this writing, the results and all potential uncertainties of the measurements have not been

comprehensively analysed and verified. Consequently, the following paragraphs discuss potential sources of discrepancies in the measurements.

The experimental test facility, as explained in Section 3.2.1, comprises two water tanks with open surfaces. This layout can introduce uncertainties regarding the conditions under which the CRPT may have been tested. Fig. 4.16 presents images from the lab, highlighting some potential sources of uncertainties in the measurements. The two images above highlight significant flow motions in the lower tank. These flow motions become particularly crucial in pump mode. This is because of the possibility of a swirling flow in the lower tank entering the CRPT via pipe 1 (see Fig. 3.3). The importance of this is amplified considering that pipe 1 is connected to the side of the lower tank, allowing swirling flows to form and be transported to the CRPT when operating in pump mode. As demonstrated in Fig. 4.12, an incoming tangential velocity has a large impact on the performance of the CRPT. Initially, the plan was to measure flow velocities using a 3-hole pressure probe in the experiments. However, because of excessive noise in the 3-hole probe measurements, it was not possible to determine the velocity components.

In turbine mode, the conditions in the upstream elevated tank are unknown because of limited accessibility. Nevertheless, the possibility of swirling flows or even a whirlpool in the elevated tank cannot be dismissed. The substantial overflow and fluid motions in the lower tank, as seen in the above right of Fig. 4.16, suggest an unstable water surface. Such an unstable water surface in the downstream tank can generate pressure oscillations within the system, thereby leading to unstable operating conditions for the CRPT.

The below left picture of Fig. 4.16 demonstrates axial clearances, or gaps, for the runners in the test facility. In the CFD models, no axial clearances are assumed since these were unknown until the test facility was built in late 2023. The gap between the runners can potentially lead to complex secondary flow patterns or high fluid shear stress between the rotating parts. Moreover, upon examining the shroud in the two images below, it is seen that the runners have touched the shroud during the experiments.

In the experimental tests, cavitation was reported to occur in both pump and turbine modes. In the below right picture of Fig. 4.16, the machine is tested in pump mode, and cavitation is clearly visible. A significant part of the suction side of the Runner 1 blades experiences cavitation, as well as tip-vortex cavitation. A smaller area of the suction side of the Runner 2 blades, near the shroud, is also experiencing cavitation. As demonstrated in Paper H, even small levels of cavitation can have a substantial impact on the performance. However, the CFD results presented in this section did not consider any cavitation.

The calculated power from the experiments is based on torque measurements. Torque transducers were positioned outside the mounting arrangement, on the shaft between the bevel gear and the motor-generator unit (see Fig. 2.1), during the experiments. To counteract drive train friction in the torque measurements, the drive train losses were measured and characterised under dry conditions by stepwise accelerating and decelerating the runners. However, the drive train losses indicated a considerable variation with the rotational speed, and colleagues reported that the torque could be off by 4% for Runner 1 and up to

7% for Runner 2 using the proposed characterisation.

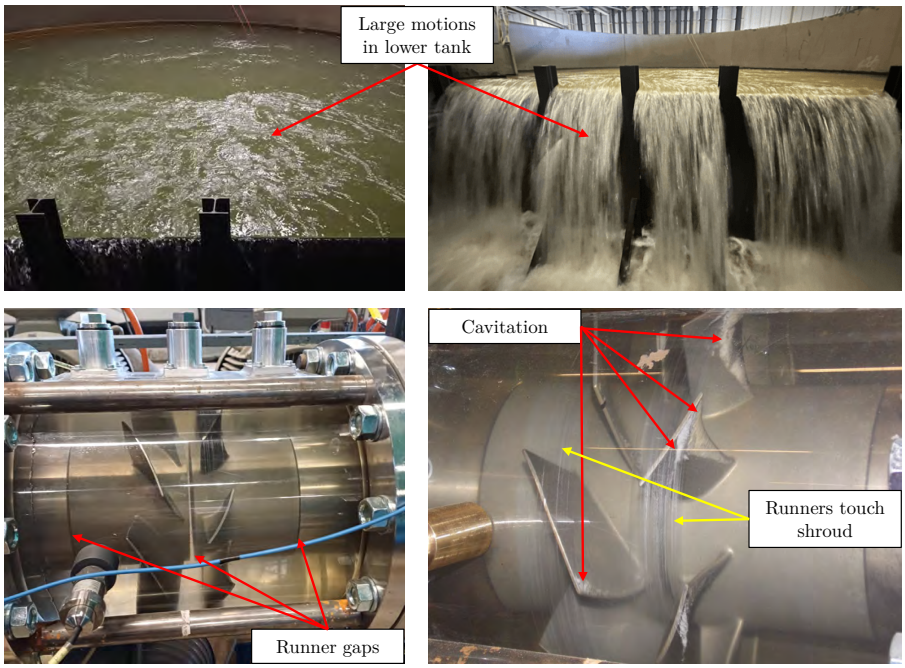

Figure 4.16: Pictures from the experiments highlighting potential sources for the discrepancies between CFD and experimental results. Above left: lower tank in pump mode, above right: lower tank overflow in turbine mode. Below left: gaps for the runners, below right: cavitation and runners touching the shroud. Note that Runner 1 is positioned to the right and Runner 2 to the left in the two below images.

Chapter 5

Summary of papers

5.1 Paper A

J. Fahlbeck, H. Nilsson, S. Salehi, M. Zangeneh, M. Joseph, Numerical analysis of an initial design of a counter-rotating pump-turbine, *IOP Conference Series: Earth and Environmental Science* **774** (1) (2021) p. 012066. DOI: 10.1088/1755-1315/774/1/012066. Conference: *30th IAHR Symposium on Hydraulic Machinery and Systems*, (Online) Lausanne, Switzerland (2021, March 21–26)

Division of work

Original draft written by Fahlbeck. Joseph created the blade geometries and performed the steady-state CFD simulations in CFX. Fahlbeck carried out all simulations in OpenFOAM and foam-extend, both steady-state and unsteady computations. All graphs and illustrations were created by Fahlbeck. All authors were responsible for reviewing the manuscript.

Summary and discussion

An initial design of the CRPT, created by Joseph, was analysed using CFD simulations at a number of stationary operating conditions in both pump and turbine modes. These simulations concerned both a prototype scale and a model scale CRPT. At the prototype scale, results were compared between the proprietary ANSYS CFX solver and the foam-extend 4.1 nextRelease open-source solver, demonstrating acceptable agreement between the two solvers. At the model scale, steady-state computations performed with foam-extend were compared to unsteady simulations using OpenFOAM v1912. The results indicated that the initial design of the CRPT could achieve hydraulic efficiencies of approximately 90% in both pump and turbine modes. The unsteady simulations were consistent with the steady-state at the design point. However, it was evident that the flow field is complex already at the design point due to rotor-rotor interaction.

5.2 Paper B

J. Fahlbeck, H. Nilsson, S. Salehi, Flow Characteristics of Preliminary Shutdown and Startup Sequences for a Model Counter-Rotating Pump-Turbine, *Energies* **14** (12) (2021) p. 3593. DOI: 10.3390/en14123593

Division of work

Original draft written by Fahlbeck. The numerical simulations, post-processing data and creation of graphs were made Fahlbeck. All authors were responsible for reviewing the manuscript.

Summary and discussion

Preliminary shutdown and startup sequences were assessed using CFD. These sequences were made based on the assumption that the flow could be controlled and regulated solely through the rotational speed of the runners. The results revealed that the sequences in pump mode were more severe than those in turbine mode. This was because larger force and torque gradients, along with peak values, were exhibited in the pump mode sequences. Based on these results, it was suggested that a valve should ideally be incorporated into the transient sequences to prevent reversed flow, thereby potentially limiting the high-amplitude loads during pump mode startup and shutdown. This recommendation was made because the largest load gradients occurred when the flow changed direction in pump mode.

5.3 Paper C

J. Fahlbeck, H. Nilsson, S. Salehi, A Head Loss Pressure Boundary Condition for Hydraulic Systems, *OpenFOAM Journal* **2** (2022) pp. 1–12. DOI: 10.51560/ofj.v2.69

Division of work

Original draft written by Fahlbeck. Development of the initial boundary condition, creation of a numerical model, and illustrations were made by Fahlbeck. Nilsson provided a test case and experimental validation data. All authors were responsible for reviewing the manuscript and the code.

Summary and discussion

A pressure boundary condition for the OpenFOAM open-source CFD code was developed in C++ and validated against available experimental test data. This boundary condition, named `headLossPressure`, incorporates the primary effects of a larger hydraulic system in terms of head or pressure losses from various components within the system, such as valves, bends, and wall friction. The head losses of the system are specified in terms of local or friction losses.

The boundary condition utilises Bernoulli's equation to adjust the pressure at the boundaries of the computational domain. It further allows for the specification of the hydrostatic head of the system and a time-varying local loss coefficient, such as a transient valve sequence. The results demonstrated that the main pressure variation and computed flow rate align closely with the validation cases.

5.4 Paper D

J. Fahlbeck, H. Nilsson, S. Salehi, Evaluation of startup time for a model contra-rotating pump-turbine in pump-mode, *IOP Conference Series: Earth and Environmental Science* **1079** (1) (2022) p. 012034. DOI: 10.1088/1755-1315/1079/1/012034. Conference: *31st IAHR Symposium on Hydraulic Machinery and Systems*, Trondheim, Norway (2022, June 26–July 1)

Division of work

Original draft written by Fahlbeck. The simulations and illustrations of results were made by Fahlbeck. All authors were responsible for reviewing the paper.

Summary and discussion

The physical time of a non-optimised startup sequence in pump mode was assessed using a low-fidelity CFD model of the CRPT. The startup sequence encompassed a valve opening and individual speedup of the two runners. It was presumed that the runners were accelerated to 61% of their nominal rotational speed with a fully closed valve, ensuring the prevention of reversed flow. The sequence commenced with the valve opening, followed by the speedup of the downstream Runner 2, and finally, the rotational speed of the upstream Runner 1 was increased. The `headLossPressure` boundary condition was employed to capture the main effects from the experimental test facility and to control the valve opening through a time-varying local loss coefficient. The results indicated that the low-fidelity CFD model adequately represented the startup sequence when compared to results from a high-fidelity CFD model. Upon evaluating the physical time of the startup sequence, it was found that a relatively fast startup time of 10 s would be sufficient to avoid surpassing the maximum permitted torque of 250 N·m. A startup sequence longer than 10 s was feasible from a load perspective. However, it was demonstrated that there was a limited benefit in extending the startup time from 20 to 30 s.

5.5 Paper E

J. Fahlbeck, H. Nilsson, S. Salehi, Surrogate based optimisation of a pump mode startup sequence for a contra-rotating pump-turbine using a genetic algorithm and computational fluid dynamics, *Journal of Energy Storage* **62** (2023) p. 106902 DOI: 10.1016/j.est.2023.106902

Division of work

Original draft written by Fahlbeck. The simulations and illustrations were made by Fahlbeck. The optimisation work was made by Fahlbeck. Salehi provided insights on how to improve the optimisation procedure. All authors were responsible for reviewing the paper.

Summary and discussion

The pump mode startup sequence was optimised using surrogate based optimisation and CFD sample points. The startup sequence was characterised by five design variables, one for the valve and two for each runner. An objective function was formulated based on the time integration of the magnitude of the gradient in time of the axial force of both runners. This objective function was mapped onto a Gaussian-process surrogate model as a function of the five design variables. The Gaussian-process surrogate model demonstrated sufficient accuracy with leave-one-out cross-validated R^2 and normalised root mean square error values. A genetic elitist algorithm was employed to find the optimal combination of the five design variables to limit low-frequency, high-amplitude loads on the runners. The optimal solution presented significantly reduced load peaks when compared to a baseline case. It was found that for the optimal startup sequence in pump mode, the valve should open during 73% of the sequence. The upstream Runner 1 should start speeding up prior to that of the downstream Runner 2. The speedup of Runner 1 should occur during most of the sequence, while Runner 2 should speed up in the final third of the sequence.

5.6 Paper F

J. Fahlbeck, H. Nilsson, S. Salehi, On the pump mode shutdown sequence for a model contra-rotating pump-turbine, *IOP Conference Series: Earth and Environmental Science*, under review. Conference: *9th IAHR Meeting of the WorkGroup on Cavitation and Dynamic Problems in Hydraulic Machinery and Systems*, Timişoara, Romania (2023, October 10–12)

Division of work

Original draft written by Fahlbeck. The simulations and illustrations of results were made by Fahlbeck. All authors were responsible for reviewing the paper.

Summary and discussion

Two pump mode shutdown sequences were evaluated to determine whether a valve should be closed before or after the runners had been brought to a standstill. It was found that closing the valve before speeding down the runners presented smoother load gradients. On the other hand, closing the valve first enlarged the pressure fluctuations during the sequence. This was because the

runners rotated at their nominal speeds while closing the valve, causing flow structures in a wide range of scales. Based on the two sequences, it was still concluded that it is preferable to close the valve before speeding down the runners as reversed flow is thereby avoided and the aforementioned smoother load gradients. Moreover, it was argued that the optimal pump mode shutdown sequence is likely a combination of the two sequences.

5.7 Paper G

J. Fahlbeck, H. Nilsson, S. Salehi, Analysis of mode-switching of a contra-rotating pump-turbine based on load gradient limiting shutdown and startup sequences, *IOP Conference Series: Earth and Environmental Science*, accepted. Conference: *32nd IAHR Symposium on Hydraulic Machinery and Systems*, Roorkee, India (2024, September 11–14)

Division of work

Original draft written by Fahlbeck. The simulations and illustrations of results were made by Fahlbeck. All authors were responsible for reviewing the paper.

Summary and discussion

Startup and shutdown sequences in both pump and turbine modes from previous studies were integrated into comprehensive mode-switching sequences and analysed using CFD. These sequences aimed to limit the load gradients during mode-switching. The pump-to-turbine sequence took 5.00 s, while the turbine-to-pump sequence required 4.95 s. The most substantial loads occurred during the pump mode parts of the mode-switching sequences. During the pump shutdown in the pump-to-turbine mode-switching, a load peak emerged on Runner 2 because of the decelerating flow rate. During the pump startup in the turbine-to-pump mode-switching, the loads on Runner 2 surpassed those at the final operating condition, indicating the importance of the nominal operating conditions when executing transient operations. This was because the optimised pump mode startup sequence from Paper E was employed. However, the nominal pump mode operating conditions were altered in this current study. In Paper E, the loads during the sequence did not exceed those at the nominal operating condition. The turbine mode sequences presented comparably smooth variations in the runner loads.

5.8 Paper H

J. Fahlbeck, H. Nilsson, S. Salehi, M. H. Arabnejad, Performance characteristics of a contra-rotating pump-turbine in turbine and pump modes under cavitating flow conditions, *Submitted for journal publication*, under review

Division of work

Original draft written by Fahlbeck. The simulations and illustrations were made by Fahlbeck. Arabnejad provided detailed insights on how to run and set up simulations for cavitating flow conditions using OpenFOAM. Salehi was responsible for the modal analysis using the dynamic mode decomposition method. All authors were responsible for reviewing the paper.

Summary and discussion

Cavitating flow conditions were evaluated in turbine and pump modes for the CRPT. The goal was to understand how and why the performance of the CRPT was affected by cavitation. In the study, the static pressure on the outlet boundary was gradually changed to induce cavitating flow conditions. In total, eight operating conditions were evaluated in each mode, and three cases in each mode were selected for an in-depth study. It was discovered that the pump mode operation was more sensitive to cavitation compared to the turbine mode. To maintain performance close to unaffected, the Thoma number (σ) needed to be above 1.5 in pump mode and 1.0 in turbine mode. It was shown that the presence of cavitation resulted in flow separation on the suction side of the Runner 1 blades, which was the main reason for the loss in performance. Furthermore, cavitation influenced the pressure pulsations close to the runners because the change in vapour volume interacted with flow separation from the support struts, which were responsible for some of the largest pressure pulsations.

Chapter 6

Concluding remarks

This PhD thesis aimed to evaluate the flow of the low-head contra-rotating pump-turbine (CRPT) developed within the ALPHEUS project at stationary, transient, and cavitating conditions. The research activities mainly focused on computational fluid dynamics (CFD) simulations of the fluid flow through the CRPT.

At stationary conditions, it has been demonstrated that the CRPT can produce a hydraulic efficiency of about 90% in both turbine and pump modes. The comparably high efficiency in both modes is because the downstream runner effectively de-swirls the flow from the upstream runner. Hence, the flow downstream of the CRPT is predominantly in the axial direction at the best efficiency conditions. The close to 90% efficiency in each mode concerns only the hydraulic efficiency of the runners. However, partners of the ALPHEUS project have estimated that the total cycle efficiency of low-head PHS with CRPTs would be around 70%. Moreover, it has been shown that the CRPT performance is sensitive to incoming swirl velocity. It is thus vital for the CRPT that the conduit and flow-control valve are constructed to minimise the risk of incoming swirl velocity.

Dominating pressure and load pulsations at both stationary and transient conditions have frequencies that correlate to the blade passing frequencies of each runner. The primary blade passing frequency of each runner is caused by the wakes from its blades. The linear combination of the blade passing frequencies of each runner typically also indicates spikes in the frequency spectrum. This spike at the linear combination frequency is an effect of the wakes from the upstream runner being cut by the downstream runner. During startup and shutdown sequences, the mentioned frequencies dominate during most of the transient operations.

It has been demonstrated that the nominal operating conditions have a large impact on the time-varying loads experienced by the runners during pump mode startup and shutdown sequences. Additionally, large force and torque spikes are experienced when transitioning between regular pump and brake modes. Thus, to avoid the brake mode, a valve is suggested to be part of the startup and shutdown sequences in pump mode. The optimal pump

mode startup consists of an initial phase where the runners speed up so the net head matches the gross head before opening the valve. As the sequence continues, the valve should open during about three-quarters of the sequence. The low-pressure runner (Runner 1) speeds up during most of the sequence, and the high-pressure runner (Runner 2) speeds up in the final third of the sequence. For a pump mode shutdown sequence that limits load gradients, it is advisable to speed down the runners concurrently with the final stages of the valve closure or even after the valve has been completely closed.

The load variations experienced in turbine mode startup and shutdown sequences are less severe compared to the corresponding pump mode operations. The main reason for this is that at a given gross head and flow rate, the pump must always deliver a higher power than what can be extracted in turbine mode. The lower power in turbine mode explains the overall lower loads experienced by the runners. Despite this, achieving favourable load gradient limit sequences in turbine mode was possible. In the turbine mode startup, the valve should start to open shortly before speeding up the runners simultaneously. In the turbine mode shutdown, a multi-stage valve closure is suggested to reduce the flow rate while speeding down the runners.

Based on this work, it has been observed that the most advantageous startup and shutdown sequences exhibit a smooth change in the flow rate for the majority of the sequence duration. This observation suggests a strategy for minimising potential detrimental load gradients during transient operations. Specifically, the change in flow rate should be as smooth as possible for as much time of the sequence as possible.

It was demonstrated that the presence of cavitating flow can negatively impact the CRPT's operating performance. The low-pressure runner experienced the worst conditions in terms of cavitation. The cavitating flow caused flow separation on the suction side of the low-pressure runner blades. The separated flow resulted in inappropriate flow guidance in the blade passages, which explained the degraded performance at cavitating flow conditions. Additionally, oscillations in cavitating regions can interact with the pressure pulsations. For instance, cavitation was observed in the wake regions of the support struts on the low-pressure side of the machine.

6.1 Further work and outlook

The differences in operating performance between numerical and experimental results should be further investigated. Because the experimental campaign in the ALPHEUS project of the CRPT was severely delayed, no complete validation of the numerical results could be performed within this thesis. Hence, the first step would be to understand the reasons behind the differences in experimental and numerical results at stationary conditions. Secondly, the suggested transient sequences from this thesis should be evaluated experimentally and numerically once the results either align or the causes for any discrepancies are comprehended. This would provide insights into the accuracy of transient CFD simulations for the CRPT. It could be noted that the colleagues who

conducted the experiments reported that they used a simplified version of the Paper E optimised pump mode startup sequence. This was because they would otherwise observe large torque gradients during the startup phase.

With the `headLossPressure` boundary condition used in the transient simulations, no inertia effects from flow acceleration are considered in the parts modelled at the boundaries. Hence, it would be useful to expand the `headLossPressure` boundary condition and include the pressure change because of unsteady inertia. According to Riedelbauch and Stens [81], the pressure difference from unsteady inertia in a pipe is calculated by the fluid mass times flow acceleration as

$$F_{\text{inertia}} = \rho A L \frac{\mathrm{d}Q/A}{\mathrm{d}t} \quad \Leftrightarrow \quad p_{\text{inertia}} = \rho \frac{L}{A} \frac{\mathrm{d}Q}{\mathrm{d}t}. \tag{6.1}$$

Here ρ is the fluid density, A and L are the cross-sectional area and length of the pipe, respectively, Q is the flow rate, and t is the time. Attempts were made to incorporate the unsteady inertia term from Eq. (6.1) into the expression used for the `headLossPressure` boundary condition, see Eq. (3.16). However, these attempts were successful only on the 1D domain used in Paper C. When it comes to the full 3D CFD simulations of the CRPT, the acceleration term ($\mathrm{d}Q/\mathrm{d}t$) causes the numerical solver to diverge. Other aspects like water hammer are not considered of interest for the `headLossPressure` since alternative approaches, for instance the method of characteristic, exist for such scenarios. It is worth noting that a colleague from the ALPHEUS project evaluated the effects of water hammer. The conclusion was that pressure spikes because of water hammer were not deemed as a problem for the suggested startup and shutdown sequences.

The present work was predominantly performed at the model scale. Therefore, evaluating the suggested startup and shutdown sequences at a prototype scale would provide insights into the scalability of transient sequences. As part of the ALPHEUS project, the time scales of the suggested sequences were scaled using the Strouhal number as [82]

$$\Delta t_{\text{p}} = \Delta t_{\text{m}} \frac{n_{\text{m}}}{n_{\text{p}}},$$

where Δt is the time scale, n is the rotational speed, and subscripts p and m are for prototype and model, respectively. Using this scaling law, it was shown that the corresponding time scales for the mode-switching sequences in Paper G would be around 110 s at the prototype scale. However, whether that time is truly appropriate remains to be evaluated as it was shown in Paper D that the time of a transient sequence largely impacts the load gradients.

Another aspect highlighted by the results in Paper G, compared to those from Papers E and F, was that the nominal conditions impacted the load gradients during the startup and shutdown sequences. It would be interesting to explore the reasons for this further and how to avoid it. The pump mode nominal condition in Paper G uses a larger gross head and different runner rotational speeds compared to the other works. A hypothesis is that because the hump zone is passed at higher rotational speeds, larger load gradients are

experienced by the runners as the flow changes between being mainly mixed to being appropriately guided through the blade passages. For a startup case, an option to avoid the Runner 2 load peak observed in Paper G would potentially be to speed up the runners to rotational speeds larger than those at the nominal condition. In such a startup sequence, the hump zone is passed at an earlier stage, as the valve opening is smaller. Once the hump zone is passed, the rotational speed of the runners could be reduced to the nominal condition. For the shutdown sequence, an option to mitigate the load peak experienced in Paper G might be to introduce a multi-stage valve closure or speed down of the runners.

Cavitation was only considered at stationary conditions in this thesis. However, it was observed in the experimental tests carried out in the ALPHEUS project, and reported in the literature, that cavitation can occur during transient operations. Therefore, transient cavitating flow simulations could be made to understand how and if cavitation impacts the suggested transient operations.

Finally, whether low-head PHS will ever be constructed and used as a viable option for large-scale energy storage remains to be uncovered. However, regardless of whether low-head PHS is built, the CRPT may have other use cases than pure energy storage. This could for instance be in tidal power plants, dry docks, sluices, or other applications where large volumes of water need to be redistributed.

Bibliography

[1] IPCC, *Climate Change 2021: The Physical Science Basis. Contribution of Working Group I to the Sixth Assessment Report of the Intergovernmental Panel on Climate Change*. Cambridge University Press, 2021 (cit. on p. 3).

[2] IRENA, *Global Renewables Outlook: Energy Transformation 2050*. International Renewable Energy Agency (IRENA), 2020, ISBN: 978-92-9260-238-3 (cit. on pp. 3, 4).

[3] IRENA, *Tracking COP28 outcomes: Tripling renewable power capacity by 2030*. International Renewable Energy Agency, 2024, ISBN: 978-92-9260-585-8 (cit. on p. 3).

[4] IEA, *Net Zero Roadmap: A Global Pathway to Keep the 1.5 °C Goal in Reach*. 2023. [Online]. Available: `https://www.iea.org/reports/net-zero-roadmap-a-global-pathway-to-keep-the-15-0c-goal-in-reach` (visited on 29th May 2024) (cit. on pp. 3, 4).

[5] *CC BY 4.0 Deed — Attribution 4.0 International — Creative Commons*. [Online]. Available: `https://creativecommons.org/licenses/by/4.0/` (visited on 5th Jun. 2024) (cit. on pp. 4, 7).

[6] H. Chen *et al.*, 'Progress in electrical energy storage system: A critical review,' *Progress in Natural Science*, vol. 19, no. 3, pp. 291–312, 2009, ISSN: 1002-0071. DOI: `10.1016/j.pnsc.2008.07.014` (cit. on pp. 3, 4).

[7] J. Mitali, S. Dhinakaran and A. A. Mohamad, 'Energy storage systems a review,' *Energy Storage and Saving*, vol. 1, no. 3, pp. 166–216, 2022, ISSN: 2772-6835. DOI: `10.1016/j.enss.2022.07.002` (cit. on pp. 3, 4, 6).

[8] H. Zhao *et al.*, 'Review of energy storage system for wind power integration support,' *Applied Energy*, vol. 137, pp. 545–553, 2015, ISSN: 0306-2619. DOI: `10.1016/j.apenergy.2014.04.103` (cit. on p. 4).

[9] M. M. Rahman *et al.*, 'Assessment of energy storage technologies: A review,' *Energy Conversion and Management*, vol. 223, p. 113 295, 2020, ISSN: 0196-8904. DOI: `10.1016/j.enconman.2020.113295` (cit. on pp. 4, 6).

[10] E. A. Kubankova and I. A. Arkharov, 'A Review of Energy Storage Systems,' *Chemical and Petroleum Engineering*, vol. 58, no. 11, pp. 936–942, 2023, ISSN: 1573-8329. DOI: 10.1007/s10556-023-01185-6 (cit. on pp. 4–6).

[11] H. E. Murdock *et al.*, 'Renewables 2021 - Global status report,' Tech. Rep. 978-3-948393-03-8, 2021, INIS-FR–21-0788, p. 603 (cit. on p. 4).

[12] IHA, *2021 Hydropower Status Report*. IHA Central Office, London, 2021. [Online]. Available: https://www.hydropower.org/publications/2021-hydropower-status-report (visited on 29th May 2024) (cit. on p. 4).

[13] IHA, *2024 World Hydropower Outlook*. IHA Central Office, London, 2024. [Online]. Available: https://www.hydropower.org/publications/2024-world-hydropower-outlook (visited on 12th Jun. 2024) (cit. on p. 4).

[14] R. Baxter, *Energy Storage - A Nontechnical Guide*. PennWell, 2007, ISBN: 978-1-59370-072-0 (cit. on p. 4).

[15] R. Ansorena Ruiz *et al.*, 'Low-head pumped hydro storage: A review on civil structure designs, legal and environmental aspects to make its realization feasible in seawater,' *Renewable and Sustainable Energy Reviews*, vol. 160, p. 112 281, 2022, ISSN: 1364-0321. DOI: 10.1016/j.rser.2022.112281 (cit. on pp. 5, 7).

[16] S. Koohi-Fayegh and M. A. Rosen, 'A review of energy storage types, applications and recent developments,' *Journal of Energy Storage*, vol. 27, p. 101 047, 2020, ISSN: 2352-152X. DOI: 10.1016/j.est.2019.101047 (cit. on pp. 5, 6).

[17] International Hydropower Association, 2024. [Online]. Available: https://www.hydropower.org/ (visited on 31st May 2024) (cit. on p. 5).

[18] M. Rogner and N. Troja, *The world's water battery: Pumped hydropower storage and the clean energy transition*. IHA Central Office, London, 2018. [Online]. Available: https://www.hydropower.org/publications/the-world-e2-80-99s-water-battery-pumped-hydropower-storage-and-the-clean-energy-transition (visited on 12th Jun. 2024) (cit. on p. 5).

[19] V. Kitsikoudis *et al.*, 'Underground Pumped-Storage Hydropower (UPSH) at the Martelange Mine (Belgium): Underground Reservoir Hydraulics,' *Energies*, vol. 13, no. 14, p. 3512, 2020, ISSN: 1996-1073. DOI: 10.3390/en13143512 (cit. on p. 5).

[20] A. G. Olabi *et al.*, 'Critical review of energy storage systems,' *Energy*, vol. 214, p. 118 987, 2021, ISSN: 0360-5442. DOI: 10.1016/j.energy.2020.118987 (cit. on p. 6).

[21] J. P. Hoffstaedt *et al.*, 'Low-head pumped hydro storage: A review of applicable technologies for design, grid integration, control and modelling,' *Renewable and Sustainable Energy Reviews*, vol. 158, p. 112 119, 2022, ISSN: 1364-0321. DOI: 10.1016/j.rser.2022.112119 (cit. on pp. 6–8).

[22] *ALPHEUS H2020*, 2024. [Online]. Available: https://alpheus-h2020.eu/ (visited on 29th May 2024) (cit. on p. 6).

[23] M. Qudaih *et al.*, 'The Contribution of Low-Head Pumped Hydro Storage to a successful Energy Transition,' in *Proceedings of the Virtual 19th Wind Integration Workshop*, 2020 (cit. on p. 6).

[24] I. J. Karassik *et al.*, *Pump Handbook, Fourth Edition*. McGraw-Hill Education, 2008, ISBN: 978-0-07-146044-6 (cit. on p. 7).

[25] A. Furukawa, T. Shigemitsu and S. Watanabe, 'Performance test and flow measurement of contra-rotating axial flow pump,' *Journal of Thermal Science*, vol. 16, no. 1, pp. 7–13, 2007, ISSN: 1993-033X. DOI: 10.1007/s11630-007-0007-4 (cit. on pp. 7, 8).

[26] Z. Qian *et al.*, 'Performance evaluation of an axial-flow pump with adjustable guide vanes in turbine mode,' *Renewable Energy*, vol. 99, pp. 1146–1152, 2016, ISSN: 0960-1481. DOI: 10.1016/j.renene.2016.08.020 (cit. on p. 7).

[27] M. Binama *et al.*, 'Investigation on pump as turbine (PAT) technical aspects for micro hydropower schemes: A state-of-the-art review,' *Renewable and Sustainable Energy Reviews*, vol. 79, pp. 148–179, 2017, ISSN: 1364-0321. DOI: 10.1016/j.rser.2017.04.071 (cit. on p. 7).

[28] I. Kougias *et al.*, 'Analysis of emerging technologies in the hydropower sector,' *Renewable and Sustainable Energy Reviews*, vol. 113, p. 109 257, 2019, ISSN: 1364-0321. DOI: 10.1016/j.rser.2019.109257 (cit. on p. 7).

[29] E. B. Prasasti *et al.*, 'Optimization of pumped hydro energy storage design and operation for offshore low-head application and grid stabilization,' *Renewable and Sustainable Energy Reviews*, vol. 191, p. 114 122, 2024, ISSN: 1364-0321. DOI: 10.1016/j.rser.2023.114122 (cit. on pp. 7, 8).

[30] S. Hötzl, 'Development of a low head axial tidal turbine,' Ph.D. dissertation, Technische Universität München, 2019 (cit. on pp. 7, 8).

[31] J.-H. Kim *et al.*, 'Design technique to improve the energy efficiency of a counter-rotating type pump-turbine,' *Renewable Energy*, vol. 101, pp. 647–659, 2017, ISSN: 0960-1481. DOI: 10.1016/j.renene.2016.09.026 (cit. on p. 8).

[32] E. B. Prasasti *et al.*, 'Design of shaft- and rim-driven contra-rotating reversible pump-turbine to optimize novel low-head pumped hydro energy storages,' *Energy*, p. 132 237, 2024, ISSN: 0360-5442. DOI: 10.1016/j.energy.2024.132237 (cit. on p. 8).

[33] E. Vagnoni *et al.*, 'Hydraulic performance evaluation of a micro-turbine with counter rotating runners by experimental investigation and numerical simulation,' *Renewable Energy*, vol. 126, pp. 943–953, 2018, ISSN: 0960-1481. DOI: 10.1016/j.renene.2018.04.015 (cit. on p. 8).

[34] J. Unterluggauer *et al.*, 'Experimental and numerical study of a prototype Francis turbine startup,' *Renewable Energy*, vol. 157, pp. 1212–1221, 2020, ISSN: 0960-1481. DOI: 10.1016/j.renene.2020.04.156 (cit. on p. 8).

[35] M. Seydoux *et al.*, 'On the prediction of the induced damage by the start-up sequence of Francis turbines: On operational resilience framework,' *Renewable Energy*, vol. 228, p. 120 587, 2024, ISSN: 0960-1481. DOI: 10.1016/j.renene.2024.120587 (cit. on p. 8).

[36] L. L. Cao *et al.*, 'On high efficiency operation of contra-rotating axial flow pump with rotational speed control toward effective energy saving,' *IOP Conference Series: Earth and Environmental Science*, vol. 15, no. 4, p. 042 027, 2012, ISSN: 1755-1315. DOI: 10.1088/1755-1315/15/4/042027 (cit. on p. 8).

[37] L. Cao *et al.*, 'Low Speed Design of Rear Rotor in Contra-Rotating Axial Flow Pump,' *International Journal of Fluid Machinery and Systems*, vol. 6, no. 2, pp. 105–112, 2013, ISSN: 1882-9554. DOI: 10.5293/IJFMS.2013.6.2.105 (cit. on p. 8).

[38] X. Liu, Y. Luo and Z. Wang, 'A review on fatigue damage mechanism in hydro turbines,' *Renewable and Sustainable Energy Reviews*, vol. 54, pp. 1–14, 2016, ISSN: 1364-0321. DOI: 10.1016/j.rser.2015.09.025 (cit. on p. 8).

[39] U. Seidel *et al.*, 'Dynamic loads in Francis runners and their impact on fatigue life,' *IOP Conference Series: Earth and Environmental Science*, vol. 22, no. 3, p. 032 054, 2014, ISSN: 1755-1315. DOI: 10.1088/1755-1315/22/3/032054 (cit. on p. 9).

[40] R. Tao *et al.*, 'Cavitation behavior study in the pump mode of a reversible pump-turbine,' *Renewable Energy*, vol. 125, pp. 655–667, 2018, ISSN: 0960-1481. DOI: 10.1016/j.renene.2018.02.114 (cit. on pp. 9, 18).

[41] S.-J. Kim *et al.*, 'Investigation of internal flow characteristics by a Thoma number in the turbine mode of a Pump–Turbine model under high flow rate,' *Renewable Energy*, vol. 199, pp. 445–461, 2022, ISSN: 0960-1481. DOI: 10.1016/j.renene.2022.08.157 (cit. on pp. 9, 18).

[42] J. B. Houdeline *et al.*, 'Start-up improvement in turbine mode for high head PSP machine,' *IOP Conference Series: Earth and Environmental Science*, vol. 15, no. 4, p. 042 022, 2012, ISSN: 1755-1315. DOI: 10.1088/1755-1315/15/4/042022 (cit. on p. 16).

[43] G. Cavazzini *et al.*, 'Unstable behaviour of pump-turbines and its effects on power regulation capacity of pumped-hydro energy storage plants,' *Renewable and Sustainable Energy Reviews*, vol. 94, pp. 399–409, 2018, ISSN: 1364-0321. DOI: 10.1016/j.rser.2018.06.018 (cit. on p. 16).

[44] G. Cavazzini *et al.*, 'Analysis of the Unstable Behavior of a Pump-Turbine in Turbine Mode: Fluid-Dynamical and Spectral Characterization of the S-shape Characteristic,' *Journal of Fluids Engineering*, vol. 138, no. 021105, 2015, ISSN: 0098-2202. DOI: 10.1115/1.4031368 (cit. on p. 16).

[45] International Electrotechnical Commission, 'IEC 60193:1999,' *Hydraulic turbines, storage pumps and pump-turbines – Model acceptance tests*, 1999 (cit. on pp. 16–18).

[46] Y. Zhang, Y. Zhang and Y. Wu, 'A review of rotating stall in reversible pump turbine,' vol. 231, no. 7, pp. 1181–1204, 2017. DOI: 10.1177/0954406216640579 (cit. on p. 16).

[47] Z. Chen *et al.*, 'Experimental and numerical study on flow instability of pump-turbine under runaway conditions,' *Renewable Energy*, vol. 210, pp. 335–345, 2023, ISSN: 0960-1481. DOI: 10.1016/j.renene.2023.04.075 (cit. on p. 16).

[48] W. M. Swanson, 'Complete Characteristic Circle Diagrams for Turbomachinery,' *Transactions of the American Society of Mechanical Engineers*, vol. 75, no. 5, pp. 819–826, 1953, ISSN: 0097-6822. DOI: 10.1115/1.4015450 (cit. on p. 17).

[49] C. E. Brennen, *Cavitation and bubble dynamics*. Oxford University Press, 1994, ISBN: 0-19-509409-3 (cit. on p. 18).

[50] H. G. Weller *et al.*, 'A tensorial approach to computational continuum mechanics using object-oriented techniques,' *Computers in Physics*, vol. 12, no. 6, p. 620, 1998. DOI: 10.1063/1.168744 (cit. on p. 19).

[51] OpenCFD, *OpenFOAM - The Open Source CFD Toolbox - User's Guide, version v1912*, OpenCFD Ltd., 2019 (cit. on p. 19).

[52] OpenCFD, *OpenFOAM - The Open Source CFD Toolbox - User's Guide, version v2012*, OpenCFD Ltd., 2020 (cit. on p. 19).

[53] F. Menter and Y. Egorov, 'A scale adaptive simulation model using two-equation models,' in *43rd AIAA aerospace sciences meeting and exhibit*, 2005, p. 1095. DOI: 10.2514/6.2005-1095 (cit. on pp. 20, 21).

[54] F. Menter and Y. Egorov, 'The Scale-Adaptive Simulation Method for Unsteady Turbulent Flow Predictions. Part 1: Theory and Model Description,' *Flow, Turbulence and Combustion*, vol. 85, no. 1, pp. 113–138, 2010, ISSN: 1573-1987. DOI: 10.1007/s10494-010-9264-5 (cit. on p. 20).

[55] F. Menter, M. Kuntz and R. Langtry, 'Ten Years of Industrial Experience with the SST Turbulence Model,' in *Fourth International Symposium on Turbulence, Heat and Mass Transfer*, vol. 4, 2003, pp. 625–632 (cit. on pp. 20, 40).

[56] Y. Egorov and F. Menter, 'Development and Application of SST-SAS Turbulence Model in the DESIDER Project,' in *Advances in Hybrid RANS-LES Modelling*, Springer, 2008, pp. 261–270, ISBN: 978-3-540-77815-8. DOI: 10.1007/978-3-540-77815-8_27 (cit. on pp. 20, 21).

[57] J. Sauer and G. H. Schnerr, 'Unsteady cavitating flow - a new cavitation model based on a modified front capturing method and bubble dynamics,' in *Proceedings of 2000 ASME fluid engineering summer conference*, vol. 251, 2000, pp. 1073–1079 (cit. on p. 21).

[58] J. Sauer, 'Instationär kavitierende Strömungen - Ein neues Modell, basierend auf Front Capturing (VoF) und Blasendynamik,' Ph.D. dissertation, Universität Karlsruhe (TH), 2000. DOI: 10.5445/IR/3122000 (cit. on p. 21).

[59] G. H. Schnerr and J. Sauer, 'Physical and numerical modeling of unsteady cavitation dynamics,' in *Fourth international conference on multiphase flow*, vol. 1, 2001 (cit. on p. 21).

[60] H. K. Versteeg and W. Malalasekera, *An introduction to computational fluid dynamics: the finite volume method*, 2nd ed. Pearson Prentice Hall, 2007, ISBN: 1-4058-9104-1 (cit. on p. 21).

[61] H. Jasak, 'Error analysis and estimation for the finite volume method with applications to fluid flows,' Ph.D. dissertation, Imperial College London, 1996 (cit. on pp. 21, 22).

[62] S. Salehi *et al.*, 'An in-depth numerical analysis of transient flow field in a Francis turbine during shutdown,' *Renewable Energy*, vol. 179, pp. 2322–2347, 2021, ISSN: 0960-1481. DOI: 10.1016/j.renene.2021.07.107 (cit. on pp. 21, 22).

[63] S. Salehi and H. Nilsson, 'Flow-induced pulsations in Francis turbines during startup - A consequence of an intermittent energy system,' *Renewable Energy*, vol. 188, pp. 1166–1183, 2022, ISSN: 0960-1481. DOI: 10.1016/j.renene.2022.01.111 (cit. on p. 21).

[64] S. Salehi and H. Nilsson, 'Effects of uncertainties in positioning of PIV plane on validation of CFD results of a high-head Francis turbine model,' *Renewable Energy*, vol. 193, pp. 57–75, 2022, ISSN: 0960-1481. DOI: 10.1016/j.renene.2022.04.018 (cit. on p. 21).

[65] H. Weller, 'Controlling the Computational Modes of the Arbitrarily Structured C Grid,' *Monthly Weather Review*, vol. 140, no. 10, pp. 3220–3234, 2012. DOI: 10.1175/MWR-D-11-00221.1 (cit. on p. 22).

[66] E. Robertson *et al.*, 'Validation of OpenFOAM numerical methods and turbulence models for incompressible bluff body flows,' *Computers & Fluids*, vol. 123, pp. 122–145, 2015, ISSN: 0045-7930. DOI: 10.1016/j.compfluid.2015.09.010 (cit. on p. 23).

[67] F. Municchi, P. P. Nagrani and I. C. Christov, 'A two-fluid model for numerical simulation of shear-dominated suspension flows,' *International Journal of Multiphase Flow*, vol. 120, p. 103 079, 2019, ISSN: 0301-9322. DOI: 10.1016/j.ijmultiphaseflow.2019.07.015 (cit. on p. 23).

[68] S. V. Patankar and D. B. Spalding, 'A calculation procedure for heat, mass and momentum transfer in three-dimensional parabolic flows,' *International Journal of Heat and Mass Transfer*, vol. 15, no. 10, pp. 1787–1806, 1972, ISSN: 0017-9310. DOI: 10.1016/0017-9310(72)90054-3 (cit. on p. 23).

[69] R. I. Issa, 'Solution of the implicitly discretised fluid flow equations by operator-splitting,' *Journal of Computational Physics*, vol. 62, no. 1, pp. 40–65, 1986, ISSN: 0021-9991. DOI: 10.1016/0021-9991(86)90099-9 (cit. on p. 23).

[70] J. Y. Luo, R. I. Issa and A. D. Gosman, 'Prediction of impeller-induced flow in mixing vessels using multiple frames of reference,' in *8th European conference on mixing*, ser. 136, Institute of Chemical Engineers Symposium Series, 1994, pp. 549–556, ISBN: 0-85295-329-1 (cit. on p. 24).

[71] M. Beaudoin *et al.*, 'Evaluation of an improved mixing plane interface for OpenFOAM,' *IOP Conference Series: Earth and Environmental Science*, vol. 22, no. 2, p. 022 004, 2014, ISSN: 1755-1315. DOI: 10.1088/1755-1315/22/2/022004 (cit. on p. 24).

[72] T. Kajishima and K. Taira, *Computational Fluid Dynamics: Incompressible Turbulent Flows*. Springer International Publishing, 2017, ISBN: 978-3-319-45304-0. DOI: 10.1007/978-3-319-45304-0_1 (cit. on p. 25).

[73] M. Zhao and M. Ghidaoui, 'Godunov-type solutions for water hammer flows,' *Journal of Hydraulic Engineering*, vol. 130, no. 4, pp. 341–348, 2004, ISSN: 0733-9429. DOI: 10.1061/(ASCE)0733-9429(2004)130:4(341) (cit. on p. 25).

[74] C. Wang and J.-D. Yang, 'Water hammer simulation using explicit-implicit coupling methods,' *Journal of Hydraulic Engineering*, vol. 141, no. 4, 2015, ISSN: 0733-9429. DOI: 10.1061/(ASCE)HY.1943-7900.0000979 (cit. on p. 25).

[75] F. M. White, *Fluid Mechanics*, 8. ed. in SI units. McGraw-Hill, 2016, ISBN: 978-981-4720-17-5 (cit. on pp. 25–27).

[76] J. P. Hoffstaedt *et al.*, 'Experimental setup and methods for a novel low-head pumped storage system,' in *IET Conference Proceedings*, IET Digital Library, 2023, pp. 341–348. DOI: 10.1049/icp.2023.1589 (cit. on p. 26).

[77] R. Tao *et al.*, 'Numerical investigation of the flow regime and cavitation in the vanes of reversible pump-turbine during pump mode's starting up,' *Renewable Energy*, vol. 141, pp. 9–19, 2019, ISSN: 0960-1481. DOI: 10.1016/j.renene.2019.03.108 (cit. on p. 30).

[78] P. Spalart and S. Allmaras, 'A one-equation turbulence model for aerodynamic flows,' in *30th Aerospace Sciences Meeting and Exhibit*, ser. Aerospace Sciences Meetings, American Institute of Aeronautics and Astronautics, 1992, p. 439. DOI: 10.2514/6.1992-439 (cit. on p. 40).

[79] D. Wilcox, 'A half century historical review of the k-omega model,' in *29th Aerospace Sciences Meeting*, American Institute of Aeronautics and Astronautics, 1991. DOI: 10.2514/6.1991-615 (cit. on p. 40).

[80] T.-H. Shih *et al.*, 'A new k-ϵ eddy viscosity model for high reynolds number turbulent flows,' *Computers & Fluids*, vol. 24, no. 3, pp. 227–238, 1995, ISSN: 0045-7930. DOI: 10.1016/0045-7930(94)00032-T (cit. on p. 40).

[81] S. Riedelbauch and C. Stens, 'Pump to turbine transient for a pump-turbine in a model test circuit and a real size power plant,' *IOP Conference Series: Earth and Environmental Science*, vol. 240, no. 7, p. 072 039, 2019, ISSN: 1755-1315. DOI: 10.1088/1755-1315/240/7/072039 (cit. on p. 57).

[82] J. Junginger, S. Riedelbauch and O. Kirschner, 'Transfer of transient conditions from prototype to closed-loop model test rig,' *IOP Conference Series: Earth and Environmental Science*, vol. 240, no. 8, p. 082 010, 2019, ISSN: 1755-1315. DOI: 10.1088/1755-1315/240/8/082010 (cit. on p. 57).